



A comparative study of different model families for the constitutive simulation of viscous clays

Merita Tafili¹ | William Fuentes² | Theodoros Triantafyllidis¹

¹Institute of Soil Mechanics and Rock Mechanics, Karlsruhe Institute of Technology, Karlsruhe 76131, Germany

²University del Norte, Km.5 Via Puerto Colombia, Barranquilla, Colombia

Correspondence

Merita Tafili, Karlsruhe Institute of Technology, Institute of Soil Mechanics and Rock Mechanics, Engler-Bunte-Ring 14, D-76131 Karlsruhe, Germany.
Email: merita.tafili@kit.edu

Summary

The simulation of the viscous behavior of some clays is of high importance in many geotechnical problems. The literature offers a vast amount of constitutive models able to simulate the rate dependence observed on these materials. Although most of these models are calibrated to very similar experimental observations and share similar definitions of material parameters, some discrepancies of their response have been detected, which are related to their mathematical formulations. In this work, the causes of these discrepancies are carefully studied. To that end, four different model families are analyzed, namely, non-stationary flow surface (NSFS) models, viscoplasticity with overstress function (OVP), viscoplasticity with Norton's power law (NVP), and visco-hypoplasticity (VHP). For the sake of a fair comparison, single constitutive models using the same set of material parameters, and following other requirements, are developed for each model family. Numerical implementations of the four resulting models are performed. Their response at different tests are carefully analyzed through simulation examples and direct examination of their constitutive equations. The set includes some basic tests at isotropic stress states and others as responses envelopes, undrained creep rupture, and an oedometer test with loading, unloading-reloading, creep, and relaxation. The article is concluded with some remarks about the observed discrepancies of these model families.

KEYWORDS

clays, NSFS, rate dependence, undrained creep rupture, visco-hypoplasticity, viscosity

1 | INTRODUCTION

Most clays show a rate-dependent mechanical behavior as presented in many experimental works.¹⁻¹¹ Experience has shown that rate dependency influences many geotechnical problems, for example, long-term settlement of structures,¹²⁻¹⁷ slope creep,^{18,19} pile shafts penetration,^{20,21} and ground anchor relaxation.²²⁻²⁶ Clearly, the study of the soil's viscous behavior is of relevant importance. Since the previous pioneer works,²⁷⁻³⁰ many empirical relations to predict some rate effects on soils have been proposed in the literature.³¹⁻³³ The consideration of these relations in the formulation of rate-dependent constitutive models has allowed users to simulate rate effects on some boundary value problems dealing with viscous clays.

Many rate-dependent models for clays are actually based on very similar fundamentals: the basis of critical state soil mechanics,^{34,35} accounting for the stress and void ratio dependence on stiffness and strength characteristics, and their

This is an open access article under the terms of the Creative Commons Attribution License, which permits use, distribution and reproduction in any medium, provided the original work is properly cited.

© 2020 The Authors. International Journal of Numerical and Analytical Methods in Geomechanics published by John Wiley & Sons Ltd.

viscous effects capabilities, adjusted to some empirical relations. In addition to this, their mathematical structure follows mostly from viscoplastic formulations, ie, the irreversible strain rate, and not, for example, the stiffness tensor, is responsible for viscous effects. With the aforementioned similarities, one may believe that two different viscous models whose formulations are adjusted to identical critical state relations, and to the same empirical relations for viscous effects, should deliver the same response. This is, however, not true: The literature offers different theoretical approaches to develop the model formulation, presenting important discrepancies between them, of which users should be aware of. One may distinguish, for example, viscous models based on nonstationary flow surface (NSFS),³⁶⁻⁴¹ viscoplastic models based on overstress functions (OVP),^{13,42-51} others based on potential laws similar to Norton's law (NVP),⁵²⁻⁵⁹ and yet recently, the so-called visco-hypoplasticity (VHP),⁶⁰ among other formulations.^{39,61,62} Model developers know that it is possible to formulate viscous models with identical material parameters but having different formulations. Works showing the capabilities of single models through predictions of experimental curves are often encountered in the literature.^{13,60,62-65} Nevertheless, very few works are devoted to compare different formulations of viscous models,^{66,67} and to the authors' knowledge, a work showing their differences directly from simulation examples is not found in the literature, probably because it would demand an exhaustive work for their formulation under the same conditions and for their numerical implementation.

The present review article aims to show the differences emerging from different model formulations for viscous clays directly from simulation examples. To that end, four different models will be proposed and implemented according to the following model families: NSFS, OVP, NVP, and VHP. In order to provide a fair comparison, they will be adjusted to the same empirical relations and calibrated with the same parameters. Most simulations presented herein do not aim to show the congruence of the models with a particular material but rather to provide simulation examples to analyze their differences due to their mathematical formulations. The selected set of model parameters follows from well-known modified Cam clay (MCC) and Buisman-type²⁷ relations. The article is structured as follows: first of all, some overall concepts often used in viscous constitutive formulations are introduced. Then, the constitutive equation for each model family is developed. These equations are adjusted to the same set of material parameters. Subsequently, the material parameters and the numerical implementations are briefly described. Several tests showing rate-effects are then simulated and carefully analyzed with the different models. The set of simulations include isotach curves, creep tests, stress relaxation tests, response envelopes, and undrained creep tests. This analysis is complemented with the simulation of an oedometric test of a Kaolin clay showing many rate effects. The article is closed with some final remarks.

2 | NOTATION AND CONVENTION

The notation and convention of the present work is as follows: Italic fonts denote scalar magnitudes (eg, a , b), bold lowercase letters denote vectors (eg, \mathbf{a} , \mathbf{b}), bold capital letters denote second-rank tensors (eg, \mathbf{A} , $\boldsymbol{\sigma}$), and special fonts are used for fourth-rank tensors (eg, E , L). Indicical notation can be used to represent components of tensors (eg, A_{ij}), and their operations follow the Einstein's summation convention. The Kronecker delta symbol is represented by δ_{ij} , ie, $\delta_{ij} = 1$ when $i = j$ and $\delta_{ij} = 0$ otherwise. The symbol $\mathbf{1}$ denotes the Kronecker delta tensor ($1_{ij} = \delta_{ij}$). The unit fourth-rank tensor for symmetric tensors is denoted by I , where $I_{ijkl} = \frac{1}{2} (\delta_{ik}\delta_{jl} + \delta_{il}\delta_{jk})$.

Multiplication with two dummy indices (double contraction) is denoted with a colon “:” (eg, $\mathbf{A} : \mathbf{B} = A_{ij}B_{ij}$). The symbol “ \otimes ” represents the dyadic product (eg, $\mathbf{A} \otimes \mathbf{B} = A_{ij}B_{kl}$). The brackets $\|\square\|$ extract the Euclidean norm (eg, $\|\mathbf{A}\| = \sqrt{A_{ij}A_{ij}}$). Normalized tensors are denoted by $\overline{\square} = \frac{\square}{\|\square\|}$ or in general as \square^{\rightarrow} . The superscript \square^{dev} extracts the deviatoric part of a tensor (eg, $\mathbf{A}^{\text{dev}} = \mathbf{A} - \frac{1}{3}(\text{tr}\mathbf{A})\mathbf{1}$). Components of the effective stress tensor $\boldsymbol{\sigma}$ or strain tensor $\boldsymbol{\varepsilon}$ in compression are negative. Roscoe variables are defined as $p = -\sigma_{ii}/3$, $q = \sqrt{\frac{3}{2}}\|\boldsymbol{\sigma}^{\text{dev}}\|$, $\varepsilon_v = -\varepsilon_{ii}$, and $\varepsilon_s = \sqrt{\frac{2}{3}}\|\boldsymbol{\varepsilon}^{\text{dev}}\|$. The stress ratio η is defined as $\eta = q/p$. The deviator stress tensor is defined as $\boldsymbol{\sigma}^{\text{dev}} = \boldsymbol{\sigma} + p\mathbf{1}$ and the stress-ratio tensor with $\mathbf{r} = \boldsymbol{\sigma}^{\text{dev}}/p = \sqrt{\frac{2}{3}}\eta\boldsymbol{\sigma}^{\text{dev}}$.

3 | CHARACTERISTIC ISOTACHS AND OVERCONSOLIDATION RATIO

In classical soil mechanics, isotropic compression yields to a unique e - p curve under normally consolidated states.²⁹ For viscous soils, a shift of this e - p line can be obtained depending on the strain rate velocity. Similar to that of other authors,^{7,30,62,68} the term “isotach” is hereafter used to denote a characteristic e - p curve related to a particular volumetric

strain rate $\dot{\epsilon}_v = \text{const}$. The $e - p$ space wherein isotachs exist is bounded according to some works. More specifically, some models consider the existence of a lower boundary at which isotachs of extremely low strain rates $\dot{\epsilon}_v \approx 0$ are bounded, or equivalently, at which creep paths cease (eg, previous studies^{43,44}). This bounding curve is in this work referred to as “minimum” isotach. Other works consider a “maximum” isotach as the upper boundary of isotachs with very high strain rates $\dot{\epsilon}_v \approx \infty$ (eg, previous studies^{38,39,41}). These and other characteristic isotachs are often used for the formulation of many existing viscoplastic models. They are summarized in the following lines:

- Reference isotach:** isotach for $\dot{\epsilon}_v = D_r$, whereby D_r is a . For the sake of convenience, the reference isotach is usually set to coincide with an experimental curve. In this work, for the case of the OVP model, the reference isotach is selected to coincide with the minimum isotach.
- Maximum isotach:** isotach for the limit value $\dot{\epsilon}_v \rightarrow \infty$. It corresponds to the upper boundary of all possible isotachs in the $e - p$ space.
- Minimum isotach:** isotach for the limit value $\dot{\epsilon}_v \rightarrow 0$. It corresponds to the lower boundary of all possible isotachs. It also bounds creep and relaxation paths under isotropic stress states ($q = 0$).
- OCR=1 isotach:** isotach at which the overconsolidation ratio under isotropic states is equal to one, ie, OCR= 1. This coincides with the definition of the normal consolidation line.

Notice that while the reference isotach is thought to match an experimental curve, the maximum and minimum isotachs are rather mathematical boundaries in the $e - p$ space. Several relations proposed in the literature are useful for their formulation, eg, previous studies.^{34,35,69-72} For instance, consider the MCC relation to describe the characteristic isotachs denoted collectively by $e = e_x(p)$:

$$e = e_x(p) = e_{x0} - \lambda \ln(p/p_r), \quad e_{x0} = \{e_{\text{ref}0}, e_{\text{max}0}, e_{\text{min}0}, e_{i0}\}, \quad (1)$$

where λ is the compression index and $e_{x0} = \{e_{\text{ref}0}, e_{\text{max}0}, e_{\text{min}0}, e_{i0}\}$ corresponds to the characteristic void ratio of the reference, maximum, minimum, and OCR= 1 isotachs at $p = p_r = 1$ kPa respectively; see Figure 1A.

One may show that the studied models in the present work can be adjusted to a reference isotach for a compression curve with $\dot{\epsilon}_v = D_r$. However, the incorporation of a maximum or a minimum isotach depends on the model type and is actually not mandatory. Particularly, the NSFS model and the VHP model incorporate only the maximum isotach in their formulations. This curve has been previously referred to as “instant normal compression line” by Yao et al³⁷ or “maximum void ratio isotach” by Fuentes et al.⁶⁰ OVP models incorporate a minimum isotach, referred to as “static yield surface” in previous studies.^{13,73,74} The NVP model is the only one incorporating neither the maximum nor the minimum isotach. It will be shown that many salient discrepancies of their response emerge from the mentioned differences.

The overconsolidation ratio in one dimension is defined as

$$\text{OCR} = \frac{p_{ei}}{p} \quad \text{with} \quad p_{ei} = \exp\left(\frac{e_{i0} - e}{\lambda}\right), \quad (2)$$

whereby p_{ei} corresponds to the Hvorslev pressure at the OCR= 1 line, solved from Equation (1). For the sake of generality, we introduce the ratio R_x , being similar to the OCR, but considering other characteristic isotachs as reference curves at which $R_x = 1$:

$$R_x = \frac{p_{e,x}}{p} \quad \text{with} \quad p_{e,x} = \exp\left(\frac{e_{i,x} - e}{\lambda}\right), \quad x = \{\text{ref}, \text{max}, \text{min}\}. \quad (3)$$

Figure 1B illustrates the Hvorslev-type variables $p_{e,x}$ at the characteristic isotachs. The definition of the overconsolidation ratio for three-dimensions, denoted hereafter with OCR_{3D} , has been differently proposed by some works, or actually omitted in others. Most authors propose a function describing a surface in the stress space at which $\text{OCR}_{3D} = 1$, represented by the condition $F_{\text{OCR}} = 0$. To keep consistency, this surface intersects the equivalent Hvorslev pressure p_{ei} at the isotropic axis, ie,

$$F_{\text{OCR}} \equiv F_{\text{OCR}}(\boldsymbol{\sigma}, p_{ei}, \dots) = 0. \quad (4)$$

For the sake of simplicity, MCC-type yield surfaces will be used for the formulation of the OCR_{3D} surface of the OVP, NVP, and NSFS models. The following MCC function $F_{\text{OCR}} = F_e$ is adopted for these models:

$$F_e = \ln\left(\frac{q^2}{M^2 p^2} + 1\right) - \ln\left(\frac{p_{ei}}{p}\right), \quad (5)$$

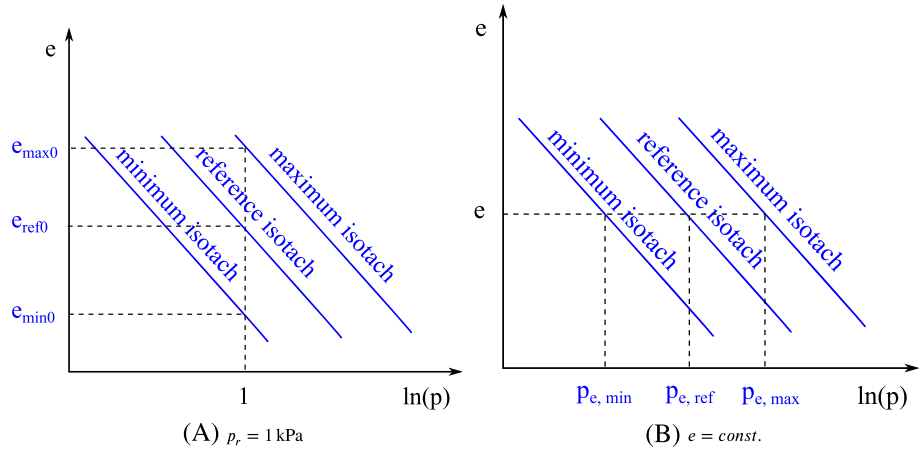


FIGURE 1 Parameters and Hvorslev pressures of characteristic isotachs

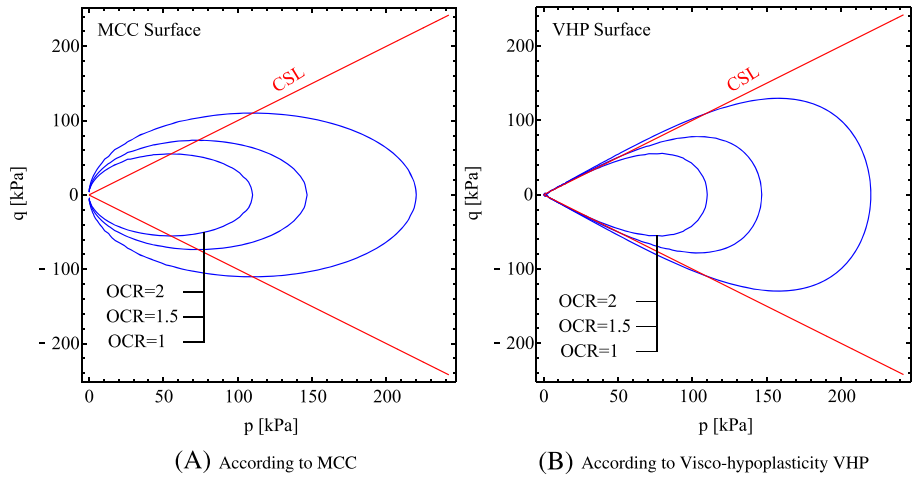


FIGURE 2 Surfaces of equal overconsolidation ratio OCR_{3D}

where M is the critical state slope in the $p - q$ space. To make our analysis simpler, we consider M a constant. However, it is strongly recommended that a Lode's angle dependence be incorporated as in other works.⁶⁰ The resulting OCR_{3D} definition being consistent with Equation (2) and (5) is

$$OCR_{3D} = \frac{p_{ei}}{p^+} \quad \text{with} \quad p^+ = p \left[1 + \left(\frac{q}{pM} \right)^2 \right], \quad (\text{MCC-type}), \quad (6)$$

whereby p^+ has been solved from Equation (5) for $F_e = 0$. An analogous relation is also used for the ratio R_x under three-dimensional states:

$$R_x = \frac{p_{e,x}}{p^+}. \quad (7)$$

OCR_{3D} functions based on different relations than MCC-type functions have been used in the literature as well. The VHP model in previous studies^{60,75} proposed a stress surface for the OCR with the following features: an open-wedge type surface that intersects the isotropic axis at $p = p_{ei}$ and the critical state surface at $p = p_{ei}/2$. The function proposed by Fuentes et al⁶⁰ reads

$$OCR_{3D} = \frac{p_{ei}}{p} + \left(1 - \frac{p_{ei}}{p} \right) \left(\frac{q}{f_b M p} \right)^2, \quad (\text{VHP - type, by Fuentes et al}^{60}), \quad (8)$$

where M is the critical state slope in the $p - q$ space, and f_b is a scalar function defined as

$$f_b = f_{b0} \left(1 - \left(\frac{e}{e_i} \right)^{n_F} \right)^{1/2}, \quad n_F = \frac{\ln((f_{b0}^2 - 1)/f_{b0}^2)}{\ln((e_i - \lambda \ln(2))/e_i)}, \quad (9)$$

and f_{b0} is considered a material constant controlling the slope of the surface at $p \rightarrow 0$ in the $p - q$ space. Accordingly, a value of approximately $f_{b0} \approx 1.1$ has been found to reproduce well many experimental observations.^{60,75} Hence, we set this value as a constant for the simulations. Figure 2 illustrates the $\text{OCR}_{3\text{D}}$ stress surfaces for MCC-type functions and the VHP model by Fuentes et al.⁶⁰

4 | CREEP RATE

Under isotropic stress conditions ($q = 0$), the creep rate describes the rate of volumetric deformation $\dot{\epsilon}_v$ upon a constant stress state $\dot{\boldsymbol{\sigma}} = \mathbf{0}$. Among many relations proposed in the literature,^{7,27,28,33} a Buisman-type relation²⁷ is selected for this work:

$$\epsilon_v = \epsilon_{v,0} - C_\alpha \ln \left(\frac{t + t_0}{t_0} \right) \quad (10)$$

whereby $\epsilon_{v,0}$ and t_0 are initial values of the void ratio and time, respectively, and C_α is analogous (but not equal) to the Buisman constant.²⁷ The differential form of Equation (10) is

$$\dot{\epsilon}_v = -C_\alpha \frac{1}{t + t_0} = C_\alpha \frac{\exp((e - e_0)/C_\alpha)}{t_0}. \quad (11)$$

Considering that creep paths are performed under constant mean pressure $\dot{p} = 0$ while a change on the Hvorslev stress p_{ei} is experienced, the difference $\epsilon - \epsilon_{v,0}$ is then related to $\epsilon_v - \epsilon_{v,0} = -\lambda \ln(p_{ei}/p) = -\lambda \ln(\text{OCR})$. One can demonstrate that substitution of the latter relation in Equation (11), and assuming that creep volumetric strains are produced by viscoplastic strains $\dot{\epsilon}_v^{\text{vis}}$, yields to the following relation:

$$\dot{\epsilon}_v^{\text{vis}} = D_r \left(\frac{1}{\text{OCR}} \right)^{1/I_v}, \quad (12)$$

where $D_r = C_\alpha/t_0$ is a reference creep rate, already introduced in other works (eg, Niemunis⁵⁵), and I_v is, by some authors, referred to as the viscosity exponent or also the Leinenkugel index,⁷⁶ which reads

$$I_v = \frac{C_\alpha}{\lambda}. \quad (13)$$

Note that $D_r = C_\alpha/t_0$ depends on the reference time $t_0 = 1$ s. This suggests that D_r is a referential factor with units of $1/\text{s}$. It can be adjusted to a particular isotach, as for example, the reference isotach. The three-dimensional extension for Equation (12) incorporates the flow rule \mathbf{m} , first referenced in Niemunis,⁵⁵ as follows:

$$\dot{\epsilon}_v^{\text{vis}} = D_r \left(\frac{1}{\text{OCR}_{3\text{D}}} \right)^{1/I_v}, \mathbf{m} \quad (14)$$

where the norm $\|\mathbf{m}\| = 1/\sqrt{3}$ has been imposed to match the behavior for 1D case in terms of \dot{p} and $\dot{\epsilon}_v$.

5 | DEVELOPMENT OF CONSTITUTIVE EQUATIONS

With the aim of performing a fair comparison, the viscous models are required to account for a set of characteristics, which are established in the following lines:

1. Isotropic compression under the reference strain rate, ie, $\dot{\epsilon}_v = D_r$, yields asymptotically to the reference isotach. Parameters $e_{\text{ref},0}$, λ , and D_r control this behavior.
2. Isotropic unloading leads to the relation $\dot{p} = p(1 + e)/\kappa \dot{\epsilon}_v$. Parameter κ must be employed.
3. Models must be able to simulate the critical state condition ($\dot{\boldsymbol{\sigma}} = \mathbf{0}$, $\dot{\epsilon}_v = 0$, $e = e_c$) at the critical state surface $q = Mp$. Parameter M defines this surface, and $e_c = e_i(p) - \lambda \ln(2)$ is the critical state void ratio.
4. The shear modulus G is proportional to the Bulk modulus K , through the relation $G = 3(1 - 2\nu)/(2(1 + \nu))K$. The Poisson ratio ν is used as parameter for this purpose.
5. Under isotropic stress conditions, a point lying at the reference isotach exhibits a creep rate equal to $\dot{\epsilon}_v = D_r(1/\text{OCR})^{1/I_v}$. The viscosity index I_v is introduced as a parameter for this purpose.

The aforementioned requirements are related to the usage of the set of parameters $\{e_{\text{ref},0}, \lambda, D_r, \kappa, M, \nu, I_v\}$ in the constitutive formulations. In the following sections, the different formulations are presented considering the aforementioned requirements.

5.1 | NSFS model

NSFS models are based on two main features: the formulation of a time-dependent yield surface responsible for the creep behavior and the consideration of the maximum isotach as the OCR = 1 isotach, ie,

$$p_{ei} = p_{e,\text{max}}, \quad \text{OCR} = R_{\text{max}}. \quad (15)$$

The model will be based on some MCC relations, as in other NSFS models in some previous studies.⁷⁷⁻⁷⁹ The Hvorslev pressure p_{ei} serves as hardening variable of the yield surface in Equation (5). It presents an isotropic hardening rule as in conventional MCC theory³⁵ with the following relation:

$$\begin{aligned} \dot{p}_{ei} &= \frac{p_{ei}}{C_p} \dot{\epsilon}_v^{\text{vp}}, \quad \text{or} \quad p_{e,\text{max}} = p_{ei0} \exp\left(\frac{\epsilon_v^{\text{vp}}}{C_p}\right), \\ C_p &= \frac{\lambda - \kappa}{1 + e_0}, \\ p_{ei0} &= \exp\left(\frac{e_{i0} - e_0}{\lambda}\right), \end{aligned} \quad (16)$$

whereby e_0 is the initial void ratio, $p_{ei0} = p_{e,\text{max}0}$ is the initial Hvorslev pressure at the maximum isotach, $e_{i0} = e_{\text{max}0}$ is the void ratio of the maximum isotach at $p = p_r = 1$ kPa, and ϵ_v^{vp} is the viscoplastic volumetric strain. An additional term $f_t = f_t(t)$ is added in Equation (5) in order to account for the time dependence of the yield surface. Following this, the time-dependent yield surface function reads

$$F_e = \ln\left(\frac{q^2}{M^2 p^2} + 1\right) - \ln\left(\frac{p_{ei}}{p}\right) + f_t. \quad (17)$$

Combination of Equations (16) and (17) in conjunction with Equation (15) yields to the following relation:

$$F_e = \ln\left(\frac{q^2}{M^2 p^2} + 1\right) + \ln\left(\frac{1}{\text{OCR}}\right) + \frac{\epsilon_v^{\text{vp}}}{C_p} + f_t. \quad (18)$$

Differentiation of Equation (18) leads to the consistency condition $\dot{F}_e = 0$:

$$\dot{F}_e = \frac{\partial F_e}{\partial \boldsymbol{\sigma}} : \dot{\boldsymbol{\sigma}} + \frac{\dot{\epsilon}_v^{\text{vp}}}{C_p} + \dot{f}_t = 0. \quad (19)$$

In order to find an expression for \dot{f}_t , the creep condition $\dot{\boldsymbol{\sigma}} = 0$ is imposed at the consistency condition $\dot{F}_e = 0$. By doing this, the following relation is obtained:

$$\dot{\epsilon}_v^{\text{vp}} = -C_p \dot{f}_t \quad (\text{for } \dot{\boldsymbol{\sigma}} = 0). \quad (20)$$

Substitution of Equations (12) and (13) in Equation (20) gives

$$\dot{f}_t = -\frac{\dot{\epsilon}_v^{\text{vp}}}{C_p} = \frac{C_\alpha \lambda}{C_p t_0} \left(\frac{1}{\text{OCR}}\right)^{1/I_v}. \quad (21)$$

The integrable form of the latter equation is $f_t = \int \dot{f}_t dt = -\epsilon_v^{\text{vp}}/C_p$. According to the Kuhn-Tucker conditions, the model is elastic for $F_e < 0$ and elasto-viscoplastic for $F_e = 0$, ie,

$$\begin{aligned} \dot{\boldsymbol{\sigma}} &= \mathbf{E} : \dot{\boldsymbol{\epsilon}} && \text{for } F_e < 0, \\ \dot{\boldsymbol{\sigma}} &= \mathbf{E} : (\dot{\boldsymbol{\epsilon}} - \dot{\boldsymbol{\epsilon}}^{\text{vp}}) && \text{for } F_e = 0, \end{aligned} \quad (22)$$

where $\dot{\epsilon}^{\text{vp}}$ is the viscoplastic strain rate tensor and E denotes the (hypo-)elastic (fourth rank) tensor, which reads

$$E = K\mathbf{1}\mathbf{1} + 2G(\mathbf{I} - \mathbf{1}\mathbf{1}/3), \quad (23)$$

where $\mathbf{1}$ is the Kronecker delta tensor, K is the Bulk modulus, and G is the shear modulus, both having MCC relations

$$K = \frac{p(1+e)}{\kappa}, \quad G = \frac{3(1-2\nu)}{2(1+\nu)}K. \quad (24)$$

The viscoplastic strain rate tensor $\dot{\epsilon}^{\text{vp}}$ follows from conventional plasticity relations:

$$\dot{\epsilon}^{\text{vp}} = \dot{\lambda}^{\text{vp}} \mathbf{m} \quad (25)$$

whereby $\dot{\lambda}^{\text{vp}}$ is the consistency parameter and \mathbf{m} is the flow rule. The consistency parameter $\dot{\lambda}^{\text{vp}}$ is solved from the consistency condition $\dot{F}_e = 0$ in conjunction with $\dot{\epsilon}_v^{\text{vp}} = -\mathbf{1} : \dot{\epsilon}^{\text{vp}}$. The solution of $\dot{\lambda}^{\text{vp}}$ can be decomposed according to

$$\dot{\lambda}^{\text{vp}} = \dot{\lambda}^{\text{pl}} + \dot{\lambda}^{\text{vis}}, \quad (26)$$

where $\dot{\lambda}^{\text{pl}}$ and $\dot{\lambda}^{\text{vis}}$ are the plastic and viscous consistency parameters, respectively, and read

$$\dot{\lambda}^{\text{pl}} = \frac{\frac{\partial F_e}{\partial \boldsymbol{\sigma}} : \mathbf{E} : \dot{\epsilon}}{\frac{\partial F_e}{\partial \boldsymbol{\sigma}} : \mathbf{E} : \mathbf{m} - \mathbf{1} : \mathbf{m}/C_p} \quad \text{and} \quad \dot{\lambda}^{\text{vis}} = \frac{\dot{f}_t}{\frac{\partial F_e}{\partial \boldsymbol{\sigma}} : \mathbf{E} : \mathbf{m} - \mathbf{1} : \mathbf{m}/C_p}. \quad (27)$$

This decomposition allows to rewrite the constitutive Equation (22) with the following form:

$$\dot{\boldsymbol{\sigma}} = \mathbf{E} : (\dot{\epsilon} - \dot{\epsilon}^{\text{pl}} - \dot{\epsilon}^{\text{vis}}), \quad (28)$$

where $\dot{\epsilon}^{\text{pl}} = \dot{\lambda}^{\text{pl}} \mathbf{m}$ and $\dot{\epsilon}^{\text{vis}} = \dot{\lambda}^{\text{vis}} \mathbf{m}$, such that $\dot{\epsilon}^{\text{vp}} = \dot{\epsilon}^{\text{pl}} + \dot{\epsilon}^{\text{vis}}$. For the sake of simplicity, the flow rule is selected to be associated with the yield surface:

$$\mathbf{m} = \frac{1}{\sqrt{3}} \left[\frac{\partial F_e}{\partial \boldsymbol{\sigma}} \right]^{\rightarrow} = \frac{1}{\sqrt{3}} \left[\frac{\partial F_e}{\partial p} \frac{\partial p}{\partial \boldsymbol{\sigma}} + \frac{\partial F_e}{\partial q} \frac{\partial q}{\partial \boldsymbol{\sigma}} \right]^{\rightarrow}. \quad (29)$$

Notice that $\|\mathbf{m}\| = 1/\sqrt{1/3}$. Similar to that of other authors,^{80,81} we distinguish between continuum Jacobian, defined as $\mathbf{J} = (\partial \dot{\boldsymbol{\sigma}})/(\partial \dot{\epsilon})$, and algorithmic Jacobian, defined as $J = (\partial \Delta \boldsymbol{\sigma})/(\partial \Delta \epsilon)$. While the first depends on the model formulation, the second depends on its numerical implementation algorithm. One may demonstrate that the continuum Jacobian \mathbf{J} of the NSFS model is similar as in classical elastoplasticity⁸⁰:

$$\mathbf{J} = \mathbf{E} - \frac{(\mathbf{E} : \frac{\partial F_e}{\partial \boldsymbol{\sigma}}) \otimes (\frac{\partial F_e}{\partial \boldsymbol{\sigma}} : \mathbf{E})}{\frac{\partial F_e}{\partial \boldsymbol{\sigma}} : \mathbf{E} : \frac{\partial F_e}{\partial \boldsymbol{\sigma}} + \mathbf{H}}, \quad (30)$$

where \mathbf{H} is the hardening modulus and reads

$$\mathbf{H} = \frac{\partial F_e}{\partial \epsilon_v^{\text{vp}}} \cdot \frac{\partial F_e}{\partial p} = \mathbf{1} : \mathbf{m}/C_p. \quad (31)$$

As an additional remark, notice that this model is able to simulate an inviscid clay by setting $I_v = 0$ because $\dot{\lambda}^{\text{vis}} = 0$; see Equation (27). For that case, the normal consolidation line would coincide with the maximum isotach.

5.2 | OVP model

According to the OVP, the total strain rate $\dot{\epsilon}$ splits into an elastic component $\dot{\epsilon}^e$ and a viscoplastic component $\dot{\epsilon}^{\text{vp}}$,^{78,82-85} that is,

$$\dot{\epsilon} = \dot{\epsilon}^e + \dot{\epsilon}^{\text{vp}} \quad (32)$$

Then, the general constitutive equation reads:

$$\dot{\boldsymbol{\sigma}} = \mathbf{E} : (\dot{\boldsymbol{\epsilon}} - \dot{\boldsymbol{\epsilon}}^{\text{VP}}). \quad (33)$$

The formulation of the (hypo-)elastic stiffness E follows from MCC relations and is identical to Equations (23) and (24). The following lines are now devoted to deduce the viscoplastic strain rate $\dot{\boldsymbol{\epsilon}}^{\text{VP}}$. Assume that the OCR = 1 isotach coincides with the minimum isotach, ie, OCR = R_{\min} and $e_{i0} = e_{\min 0}$. Considering this assumption, the yield surface function under isotropic states ($q = 0$) reads

$$F_e \equiv \ln(p/p_{e,\min}) = 0 \quad \text{for } q = 0. \quad (34)$$

We now demonstrate that the function $\exp(F_e/I_v - 1)$ is proportional to the viscoplastic strain rate $\dot{\boldsymbol{\epsilon}}_v^{\text{VP}} \sim (1/\text{OCR})^{1/I_v}$ under isotropic stress states ($q = 0$); see Equation (12). Evaluation of function $\exp(F_e/I_v - 1)$ yields to the following relation:

$$\exp\left(\frac{F_e}{I_v} - 1\right) = \exp\left(\frac{1}{I_v} \ln\left(\frac{p}{p_{e,\min}}\right) - 1\right) = 0 \quad (35)$$

$$= \exp\left(\ln\left(\frac{p}{p_{e,\min}}\right)^{1/I_v} - 1\right) = 0. \quad (36)$$

For typical values of $1/I_v > 10$, one may show that when $p > p_{e,\min}$, the approximation $\ln(p/p_{e,\min})^{1/I_v} - 1 \approx \ln(p/p_{e,\min})^{1/I_v}$ holds. Using the mentioned approximation in Equation (35), in conjunction with OCR = R_{\min} , gives

$$= \exp\left(\ln\left(\frac{p}{p_{e,\min}}\right)^{1/I_v} - 1\right) \approx \exp\left(\ln\left(\frac{p}{p_{e,\min}}\right)^{1/I_v}\right) \quad (37)$$

$$= \left(\frac{1}{\text{OCR}}\right)^{1/I_v}. \quad (38)$$

The last equation proves that $\exp(F_e/I_v - 1) \sim (1/\text{OCR})^{1/I_v}$. In light of this demonstration, OVP models adopt the following relation for $\dot{\boldsymbol{\epsilon}}^{\text{VP}}$:

$$\dot{\boldsymbol{\epsilon}}^{\text{VP}} = \phi \mathbf{m} = D_r \langle \exp\left(\frac{1}{I_v} F_e\right) - 1 \rangle, \mathbf{m} \quad (39)$$

where D_r is a parameter described in Section 4 and ϕ is often referred to as the “functional of overstress”⁴⁴ or the “viscous nucleus”. Once more, an associated flow rule has been adopted and reads

$$\mathbf{m} = \frac{1}{\sqrt{3}} \left[\frac{\partial f}{\partial \boldsymbol{\sigma}} \right]^{\top}. \quad (40)$$

Considering that the viscoplastic strain rate $\dot{\boldsymbol{\epsilon}}^{\text{VP}}$ does not depend (explicitly) on the strain rate $\dot{\boldsymbol{\epsilon}}$, the continuum Jacobian J of the OVP model simplifies to

$$\mathbf{J} = \mathbf{E}. \quad (41)$$

5.3 | Visco-plastic model with Norton's power law

Viscoplastic models with Norton's power law are very often used in the literature.^{7,13,52,55,59,62,86} The main difference of their formulation with respect to the others is the fact that they do not incorporate any boundary isotach. Its formulation is very simple and is explained in the following lines.

The general constitutive equation reads

$$\dot{\boldsymbol{\sigma}} = \mathbf{E} : (\dot{\boldsymbol{\epsilon}} - \dot{\boldsymbol{\epsilon}}^{\text{VP}}), \quad (42)$$

whereby E follows the MCC relations according to Equations (23) and (24). The viscoplastic strain rate $\dot{\boldsymbol{\epsilon}}^{\text{VP}}$ is proposed to be proportional to the Norton's power law, yet demonstrated in Equation (14):

$$\dot{\boldsymbol{\epsilon}}^{\text{VP}} = D_r \left(\frac{1}{\text{OCR}_{3D}} \right)^{1/I_v} \mathbf{m} \quad (43)$$

The overconsolidation ratio is determined through the relation given in Equation (6). Note that for highly overconsolidated states $OCR \gg 1$, the viscoplastic strain rate is negligible $\dot{\epsilon}^{vp} \approx \mathbf{0}$, and the model becomes practically (hypo-)elastic. Once more, an associated flow rule \mathbf{m} is adopted:

$$\mathbf{m} = \frac{1}{\sqrt{3}} \left[\frac{\partial f}{\partial \boldsymbol{\sigma}} \right]^{\rightarrow} \quad (44)$$

Similar to the OVP model, the continuous modulus is equal to the elastic stiffness tensor, ie, $J = E$.

5.4 | VHP model

VHP models assume a strain rate decomposition into three strain rate components as follows:

$$\dot{\epsilon} = \dot{\epsilon}^e + \dot{\epsilon}^{hp} + \dot{\epsilon}^{vis}, \quad (45)$$

whereby $\dot{\epsilon}^e$ is the elastic strain rate, $\dot{\epsilon}^{hp}$ is the hypoplastic strain rate, and $\dot{\epsilon}^{vis}$ is the viscous strain rate. In contrast to other formulations, these three components are always active and are not subjected to any yield constraint. Accordingly, the constitutive equation reads

$$\begin{aligned} \dot{\boldsymbol{\sigma}} &= \mathbf{E} : (\dot{\epsilon} - \dot{\epsilon}^{hp} - \dot{\epsilon}^{vis}), \\ &= \mathbf{E} : (\dot{\epsilon} - \dot{\epsilon}^{hp}) + \dot{\boldsymbol{\sigma}}^{vis}, \end{aligned} \quad (46)$$

whereby $\dot{\boldsymbol{\sigma}}^{vis} = -\mathbf{E} : \dot{\epsilon}^{vis}$ is the viscous stress rate and E is the (hypo-)elastic stiffness, defined as

$$\mathbf{E} = 3K\mathbf{1}\mathbf{1} + 2G(\mathbf{1} - \mathbf{1}\mathbf{1}/3) - \frac{K}{\sqrt{3}M}(\mathbf{r}\mathbf{r} + \mathbf{r}\mathbf{1}). \quad (47)$$

The factors K and G are the bulk and shear modulus, and $\mathbf{r} = \boldsymbol{\sigma}^*/p$ is the stress ratio. The bulk modulus K and shear modulus G are the same presented by Fuentes et al,⁸⁷ adjusted to match the MCC relations:

$$K = \frac{p}{\lambda} \frac{(1+e)}{(1-Y_{0m})} \quad \text{with} \quad Y_{0m} = (\lambda - \kappa)/(\lambda + \kappa), \quad (48)$$

$$G = \frac{(1-2\nu)}{2(1+\nu)}K. \quad (49)$$

The strain rate components $\dot{\epsilon}^{hp}$ and $\dot{\epsilon}^{vis}$ are defined by the following relations:

$$\dot{\epsilon}^{hp} = Y \|\dot{\epsilon}\| \mathbf{m} \quad (50)$$

$$\dot{\epsilon}^{vis} = \frac{I_v \lambda}{t_0} \left(\frac{1}{OCR_{3D}} \right)^{1/I_v} \mathbf{m} \quad (51)$$

with Y being a scalar function termed the degree of nonlinearity,⁵⁵ and the overconsolidation ratio OCR_{3D} according to Equation (8). The degree of nonlinearity Y reads

$$Y = Y_0 + (1 - Y_0) \left(\frac{\|\mathbf{r}\|}{\|\mathbf{r}_c\|} \right)^2, \quad Y_0 = Y_{0m} \left(\frac{p}{p_{e,max}} \right)^2. \quad (52)$$

where $\mathbf{r}_c = \sqrt{2/3} M_c \vec{\mathbf{r}}$. One may notice that the maximum isotach with $OCR = R_{max}$ and therefore $e_{i0} = e_{max0}$ is implemented.

Finally, the visco-hypoplastic flow rule \mathbf{m} reads

$$\mathbf{m} = \frac{1}{\sqrt{3}} \left[-\frac{1}{2} (\|\mathbf{r}_c\| - \|\mathbf{r}\|) \mathbf{1} + \frac{\mathbf{r}}{\|\mathbf{r}_c\|} \right]^{\rightarrow}. \quad (53)$$

Notice that one may simplify the constitutive model to different formulations according to the problem of interest. For example, for models specializing on monotonic loading without viscous effects, one may use the assumption $I_v = 0$, which reduces the above model to a hypoplastic model for inviscid clay. The continuous modulus J is computed similar to conventional hypoplastic models:

$$J = E - Y(E : \mathbf{m}) \otimes \vec{\epsilon}. \quad (54)$$

6 | ADJUSTMENT TO A UNIQUE REFERENCE ISOTACH

One of the requirements of the present study is that all models are adjusted with identical reference isotach. Let the reference isotach be the curve described by the equation

$$e = e_{\text{ref}0} - \lambda \ln(p/p_r). \quad (55)$$

Differentiation of Equation (55) in conjunction with the condition $\dot{\epsilon}_v = D_r$ leads to the relation

$$\dot{p} = \frac{p(1+e)}{\lambda} \dot{\epsilon}_v = \frac{p(1+e)}{\lambda} D_r. \quad (56)$$

Let us now simplify the constitutive equations of the NSFS, OVP, and NVP models, for isotropic stress states $q = 0$ subjected to a reference strain rate compression $\dot{\epsilon}_v = D_r$. According to Equations (22), (33), and (42), the following simplified forms of these models for $q = 0$ and $\dot{\epsilon}_v = D_r$ read

$$\dot{p} = K (D_r - \dot{\epsilon}_v^{\text{vp}}) = \frac{p(1+e)}{\lambda} D_r \quad (\text{NSFS, OVP, and NVP model}). \quad (57)$$

The particular case of the Visco-hypoplastic model is treated apart considering the nonlinearity of the hypoplastic strain rate $\dot{\epsilon}^{\text{hp}}$ with the strain rate, ie, $\dot{\epsilon}^{\text{hp}} \sim \|\dot{\epsilon}\|$. Its simplified form under the aforementioned conditions is

$$\dot{p} = K (D_r - Y_0 D_r - \dot{\epsilon}_v^{\text{vis}}) = \frac{p(1+e)}{\lambda} D_r \quad (\text{VHP model}). \quad (58)$$

Substitution of $\dot{\epsilon}_v^{\text{vp}}$, $\dot{\epsilon}_v^{\text{vis}}$, K , and Y_0 with their respective definitions (see Section 5) yields to the following relations:

$$\frac{1}{\kappa} \left[D_r - \frac{D_r/\kappa + I_v \lambda (\text{OCR})^{2-1/I_v}}{1/\kappa + (\text{OCR})^2/(\lambda - \kappa)} \right] = \frac{D_r}{\lambda} (\text{NSFS model}), \quad (59)$$

$$\frac{1}{\kappa} \left[D_r \left(1 - \left(\left(\frac{1}{\text{OCR}} \right)^{1/I_v} - 1 \right) \right) \right] = \frac{D_r}{\lambda} (\text{OVP model}), \quad (60)$$

$$\frac{1}{\kappa} \left[D_r \left(1 - \left(\frac{1}{\text{OCR}} \right)^{1/I_v} \right) \right] = \frac{D_r}{\lambda} (\text{NVP model}), \quad (61)$$

$$\frac{1}{1 - Y_{0m}} \left[D_r \left(1 - Y_{0m} \left(\frac{1}{\text{OCR}} \right)^2 \right) - I_v \lambda \left(\frac{1}{\text{OCR}} \right)^{1/I_v} \right] = D_r (\text{VHP model}). \quad (62)$$

The resulting equations depend on the OCR at the reference isotach. Notice that the value of OCR can be directly solved for the OVP and NVP models, from Equations (60) and (61), respectively, as follows:

$$\text{OCR} = \left(2 - \frac{\kappa}{\lambda} \right)^{-I_v} \quad (\text{OVP model}), \quad (63)$$

$$\text{OCR} = \left(1 - \frac{\kappa}{\lambda} \right)^{-I_v} \quad (\text{NVP model}). \quad (64)$$

Hence, the normal consolidation line ($\text{OCR} = 1$) corresponds nearly to the reference isotach for the OVP and the NVP model. In contrast, simple numerical methods are required for the solution of OCR for the NSFS and VHP models, ie,

Description		Units	Approx. Range	Req. Test
MCC-type parameters				
λ	Compression index	[-]	10^{-6} to 1	ICT*
κ	Swelling index	[-]	10^{-7} to 0.1	ICT
$e_{\text{ref}0}$	Void ratio at $p = 1$ kPa (RI**)	[-]	0.5 to 10	ICT
M	CS slope	[-]	0.5 to 1.5	TCT***
ν	Poisson modulus	[-]	0.0 to 0.5	TCT
Viscosity parameters				
I_v	Viscosity index	[-]	0 to 0.1	$2 \times \dot{\epsilon}$ ICT
D_r	Reference strain rate	[1/s]	10^{-12} to 10^{-3}	ICT

TABLE 1 Material parameters of the models

Abbreviations: ICT, isotropic compression test; RI, reference isotach; TCT, triaxial compression test.

Equations (59) and (62), respectively. Once the OCR is solved, the position of the OCR = 1 isotach of the different models is adjusted through parameter e_{i0} , which can be solved from the condition

$$e_{i0} = e_{\text{ref}0} - \lambda \ln \left(\frac{1}{\text{OCR}} \right). \quad (65)$$

With this method, all models are adjusted to have the same reference isotach.

Note that the normal consolidation line of the NSFS and the VHP model corresponds to their maximum isotache, as also depicted respectively in Sections 5.1 and 5.4. Hence, in order to back-fit an experiment result of OCR = 1 line (corresponding to a strain rate used in the experiment), different models require different reference strain rates, obeying Equations (59) to (62). Hence, instead of OCR, Equations (59) to (62) can be solved for D_r and then the parameter e_{i0} corresponds to $e_{i0} = e_{\text{ref}}$.

7 | MATERIAL PARAMETERS

The four models were formulated with the same set of material parameters. In total, seven parameters are required for their calibration. They are subdivided in those related to the MCC theory and those describing the viscous behavior. The MCC parameters correspond to compression index λ , the swelling index κ , the void ratio at the reference isotach $e_{\text{ref}0}$, the critical state slope M in the $p - q$ space, and the Poisson ratio ν . The additional two parameters controlling the viscous behavior correspond to the viscosity index I_v and the reference strain rate D_r . Detailed description of the procedure for their determination is encountered in Hadzibeti⁸⁸ and other works. However, in Appendix A, some hints are given for their calibration. Table 1 lists the required parameters, with their respective names, approximate range, and some suggested tests for their determination. In summary, two isotropic compression tests with different strain velocities and one triaxial compression test are required as minimum to calibrate all parameters. Obviously, a higher number of tests increases the calibration quality.

8 | NUMERICAL IMPLEMENTATION

All constitutive models were implemented in a FORTRAN subroutine as “User Material” (UMAT), compatible with the software ABAQUS Standard.⁸⁹ A substepping scheme was adopted for all implementations to avoid numerical issues. Very small substepping sizes in order of $\|\Delta \epsilon\| = 10^{-5}$ were selected to assure numerical convergence. In addition, some numerical recommendations for viscous models pointed in previous studies^{55,62,90} were considered for the OVP, NVP, and VHP models. Specifically, while the viscous strain rate was semi-implicitly integrated, other components of the models were explicitly computed. This required the computation of an algorithmic Jacobian J^{alg} , which is explained in the sequel. Numerical integration of the models under different paths assuming element test conditions (homogeneous field for stresses and strains) was solved with the use of a Newton-Raphson solution scheme, whereby tolerances and a maximum number of iterations were specified to minimize the numerical error. For the NSFS model, an elastic predictor was always computed to evaluate if an elastic or rather a viscoplastic step should be performed, as in Simo and Hughes.⁹¹ At each viscoplastic step, a small correction was applied to the stress increment $\Delta \sigma$ to assure the condition $F_e = 0$ at the end of the increment. Other models were directly implemented without distinguishing between elastic and viscoplastic steps due to the lack of a yield surface. All implementations showed rapid convergence, and no numerical issues were detected. All

the subroutine UMAT are now available for their use in finite element computations. The algorithmic Jacobians of the different models were found as follows.

The NSFS model has been explicitly integrated with a substepping technique. Hence, the algorithmic Jacobian J^{alg} has been set equal to the continuum Jacobian J (see Equation 30), ie, $J^{alg} = J$. For the OVP and NVP models, a semi-implicit integration for the viscous stress increment $\Delta\sigma^{vis}$ has been implemented. The stress increment $\Delta\sigma$ is therefore computed according to the following mathematical procedure:

$$\begin{aligned}\Delta\sigma &= \mathbf{E} : \Delta\epsilon - \mathbf{E} : \left[\dot{\epsilon}^{vis} \Delta t + \frac{1}{2} \frac{\partial \dot{\epsilon}^{vis}}{\partial \sigma} : \Delta\sigma + \frac{1}{2} \frac{\partial \dot{\epsilon}^{vis}}{\partial \dot{\epsilon}} : \Delta\dot{\epsilon} \right] \\ &\Rightarrow \left[\mathbf{I} + \frac{1}{2} \mathbf{E} : \frac{\partial \dot{\epsilon}^{vis}}{\partial \sigma} \right] : \Delta\sigma = \mathbf{E} : \Delta\epsilon - \mathbf{E} : \dot{\epsilon}^{vis} \Delta t - \frac{1}{2} \mathbf{E} : \frac{\partial \dot{\epsilon}^{vis}}{\partial \dot{\epsilon}} : \Delta\dot{\epsilon} \\ &\Rightarrow \Delta\sigma = \left[\mathbf{I} + \frac{1}{2} \mathbf{E} : \frac{\partial \dot{\epsilon}^{vis}}{\partial \sigma} \right]^{-1} : \left[\Delta\sigma^{exp} - \frac{1}{2} \mathbf{E} : \frac{\partial \dot{\epsilon}^{vis}}{\partial \dot{\epsilon}} : \Delta\dot{\epsilon} \right],\end{aligned}\quad (66)$$

where the explicit stress increment $\Delta\sigma^{exp}$ is computed as

$$\Delta\sigma^{exp} = \mathbf{E} : \Delta\epsilon - \mathbf{E} : \dot{\epsilon}^{vis} \Delta t \quad (\text{OVP and NVP model}). \quad (67)$$

The required derivatives $(\partial \dot{\epsilon}^{vp})/(\partial \sigma)$ and $(\partial \dot{\epsilon}^{vis})/(\partial \dot{\epsilon})$ are given in Appendix B. A similar integration scheme has been also performed with the VHP model. The only difference with Equation (66) is the computation of the explicit stress increment $\Delta\sigma^{exp}$, which, according to Equation (46), reads as

$$\Delta\sigma^{exp} = \mathbf{E} : \Delta\epsilon - \mathbf{E} : \dot{\epsilon}^{hp} - \mathbf{E} : \dot{\epsilon}^{vis} \Delta t \quad (\text{VHP model}) \quad (68)$$

9 | ELEMENT TEST SIMULATIONS

In this section, a set of element test simulations are presented to analyze the performance of the different model families. These simulations aim to show the distinct responses of the models under different conditions. Firstly, a set of illustrative element tests are analyzed, ie, they are not calibrated to any particular material. The selected parameters are typical on some clay-like soils and are listed in Table 2. The mathematical procedure in Section 6 was followed to adjust all models to the same reference isotach, being characterized by the set of parameters e_{ref0} , λ , and D_r . According to Section 6, the selection of a unique reference isotach for all models implies that they present different $\text{OCR} = 1$ isotachs. Therefore, the resulting characteristic void ratios e_{i0} , describing the $\text{OCR} = 1$ isotach, were computed for each particular model according to the relations given in Section 6. The values of e_{i0} are listed in Table 3. The illustrative simulations correspond to some tests showing strain rate dependency. They include isotropic compression tests with different strain rates, creep tests, relaxation tests, oedometric tests, and undrained creep tests. In addition, responses envelopes analysis⁹² were included as well to analyze the models performance on different strain/stress rate directions. Response envelopes will allow to detect directions at which viscoplastic effects act the most.

At the end, simulations of two experiments are included, the first consisting of an undrained triaxial test with tertiary creep and the second of an oedometric test with different strain rate, creep, and relaxation stages.

TABLE 2 Material parameters for the simulations

Parameters	λ	κ	M	ν	I_v	e_{ref0}	D_r
Units	[-]	[-]	[-]	[-]	[-]	[-]	[1/s]
Illustrative tests	0.1	0.02	1.0	0.25	0.04	1.2	10^{-6a} , 10^{-10b}
UTCT ^c							
NSFS	0.15	0.025	1.29	0.25	0.038	1.2	10^{-4}
OVP	0.15	0.025	1.29	0.25	0.04	1.2	4.5×10^{-4}
NVP ^d	0.15	0.025	1.29	0.25	0.05	1.2	10^{-4}
VHP	0.15	0.025	1.29	0.25	0.042	1.2	10^{-4}
Oedometric test	0.76	0.07	1.35	0.25	0.06	6.3	10^{-10}

^a for NSFS, NVP, and VHP. ^b for OVP. ^c Undrained Triaxial Creep Tests. ^d NVP model with the modification proposed by Vermeer & Neher.⁵⁹

Model	Illustrative Tests	Oedometric
NSFS model	1.234	7.24
OVP model	1.197	6.32
NVP model	1.201	6.74
VHP model	1.239	7.275

TABLE 3 Void ratio e_{i0} (at $p = 1$ kPa for the OCR= 1 isotach)

9.1 | Isotropic compression with constant strain rate

Simulations of isotropic compression tests with different volumetric strain rates $\dot{\epsilon}_v$ were performed. These simulations cataloged as basic, allow us to obtain an overview of the isotach boundaries acting at each model. Volumetric strain rates ranging between $\dot{\epsilon}_v = \{10^{-1}, 10^{-10}\}$ 1/s were systematically applied to generate different compression paths. Figure 3 presents the simulations of the NSFS, OVP, NVP, and VHP models. They show that under reference strain rate $\dot{\epsilon}_v = D_r$, yield to the reference isotach $e = 1.2 - 0.1 \ln(p)$, as a result of considering the procedure described in Section 6. The figures show that the compression curves of the NSFS and VHP models are bounded by maximum isotachs, which are different for each model. The isotachs of the OVP and NVP models are bounded by their elastic response at very high velocities, with slope equal to κ . This upper bound actually depends on the initial conditions of e and p and has been previously referred to as “instant time line” by other authors.^{37,66} Simulations with the OVP model show that a lower bound exists because of the consideration of a minimum isotach. Below this curve, the existence of isotachs for this model is not possible. But this does not have to be necessarily a negative point, because the lower bound can be shifted by choosing a very low reference creep rate D_r .

One of the reasons to use a minimum isotache is to limit the creep deformation at an infinitely long time, even though this is not proven by experimental evidence yet, but it is not refuted either. Its definition requires an additional parameter, such as R_{\min} . The problem is that an infinitely long time test is needed for its calibration. Otherwise, special procedures can be developed in order to determine this parameter like the construction of prototype models for the considered geotechnical problem whereby the final creep rate can be derived as a function of time. Note that in the literature, it is controversial whether the creep reaches a final value or not. In the current paper, the minimum isotache for OVP simply corresponds to the reference isotache line, which is not always the case. Some applications, such as problems dealing with very long time, may be disadvantageous because the creep is limited. Yet, for issues with aging effects, the introduction of this isotache may be rendered as convenient.

The maximum isotach has been introduced into some models, because it is inferred that above the normal consolidated state OCR = 1, there must be a compression line for which the creep time is “0.”³⁷ The line then describes the normally and instantaneously compressed behavior of clays, thus the name “instant normal compression line.” For geotechnical analysis, engineers may be used to have a bound of the void ratio, which implies a bound of the stress ratio, as otherwise macro pores and their impact on the constitutive modeling should be treated. Because these effects are not subject of the models described here, we find it appropriate to introduce a maximum bound of isotachs. The attentive reader may believe that the introduction of a maximum isotache may not be sufficient for installations (shaking) or especially very fast earthquakes. Yet, both the NSFS and the VHP model reach the maximum isotach for $\dot{\epsilon} \rightarrow \infty$, hence every strain rate (even very fast loading) is considered.

Figure 4 presents the resulting mean stress p at a given void ratio $e = \text{const}$ for different strain rate velocities. In particular, Figure 4A presents the results for a void ratio of $e = 1.15$ and shows that while the NSFS and the VHP model have yet not reached the maximum isotach at high velocities, the OVP model has already reached the minimum isotach at low velocities. The NSFS and VHP reach their maximum isotach at a void ratio of $e \approx 1.0$, as shown in Figure 4B.

The stress ratio, namely, the overconsolidation ratio OCR reached at the different isotachs, is depicted in Figure 5. The figure shows that while the NSFS and VHP models show values of $p_{ei}/p \geq 1$, the OVP model shows always $p_{ei}/p \leq 1$. The NVP model does not show any bound for the stress ratio p_{ei}/p . For geotechnical analysis, engineers may be used to have a bound of the void ratio, which implies a bound of the stress ratio, as otherwise macro pores and their impact on the constitutive modeling should be treated. However, these effects are not subject of the models described here. Worthy to note is also the fact that the models normal consolidation line (OCR=1) corresponds to different strain rates, hence isotachs, for each model. While for the OVP and NSFS model the OCR = 1 line corresponds to the reference isotache, for the VHP and NSFS models, the maximum isotache corresponds to the normal consolidation line OCR=1; see also Figure 5.

Examination of the constitutive equations allow us to determine the relations describing the isotach formulation. In the following lines, relations depending on the void ratio e , mean pressure p , and strain rate $\dot{\epsilon}_v$, are found to describe the

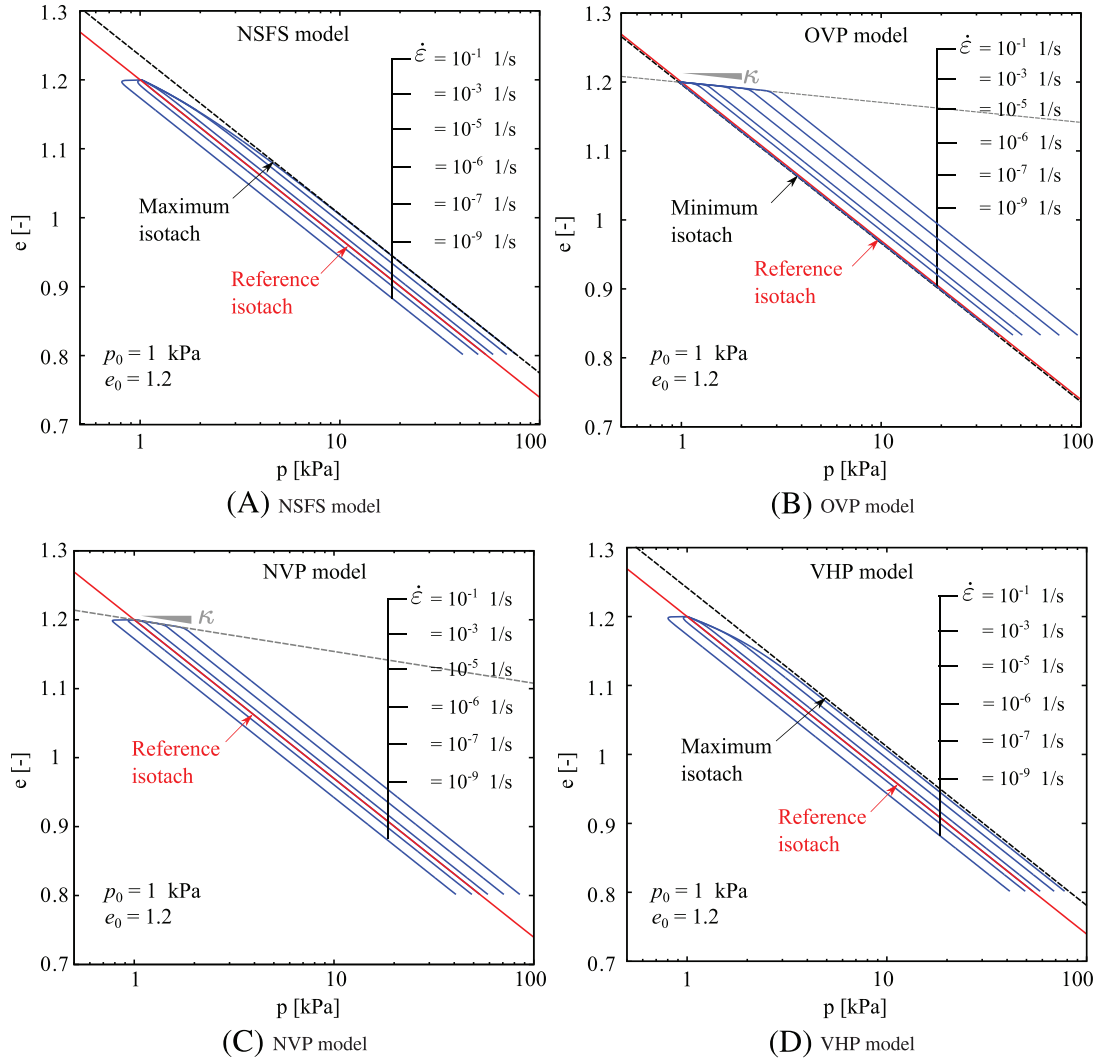


FIGURE 3 Simulations with different strain rates (isotachs)

isotach behavior for each model. The isotach curves under isotropic compression ($q = 0$) are described by the relation $\dot{p} = p(1 + e)/\lambda \dot{\epsilon}_v$. In the following lines, the relations describing the isotach curves are found for each model. Let us evaluate the constitutive equations of the NVP and OVP models for the isotach condition

$$\dot{p} = \frac{p(1 + e)}{\kappa} (\dot{\epsilon}_v - \dot{\epsilon}_v^{vp}) = \frac{p(1 + e)}{\lambda} \dot{\epsilon}_v, \quad (\text{NVP model}). \quad (69)$$

From Equation (69), one can show that from the constant strain rate condition $\ddot{\epsilon}_v = 0$ results the following relation:

$$\frac{\dot{\epsilon}_{v,a}}{\dot{\epsilon}_{v,b}} = \frac{\dot{\epsilon}_{v,a}^{vp}}{\dot{\epsilon}_{v,b}^{vp}}, \quad (70)$$

where the subindices a and b denote two different isotachs. Substitution of the corresponding definitions of $\dot{\epsilon}_v^{vp}$ for the NVP and OVP models in Equation (70) leads to the relations

$$\frac{\dot{\epsilon}_{v,a}}{\dot{\epsilon}_{v,b}} = \left(\frac{\text{OCR}_b}{\text{OCR}_a} \right)^{1/I_v} \quad (\text{NVP model}), \quad (71)$$

$$\frac{\dot{\epsilon}_{v,a}}{\dot{\epsilon}_{v,b}} = \frac{(\text{OCR}_b)^{1/I_v} - 1}{(\text{OCR}_a)^{1/I_v} - 1} \quad (\text{OVP model}). \quad (72)$$

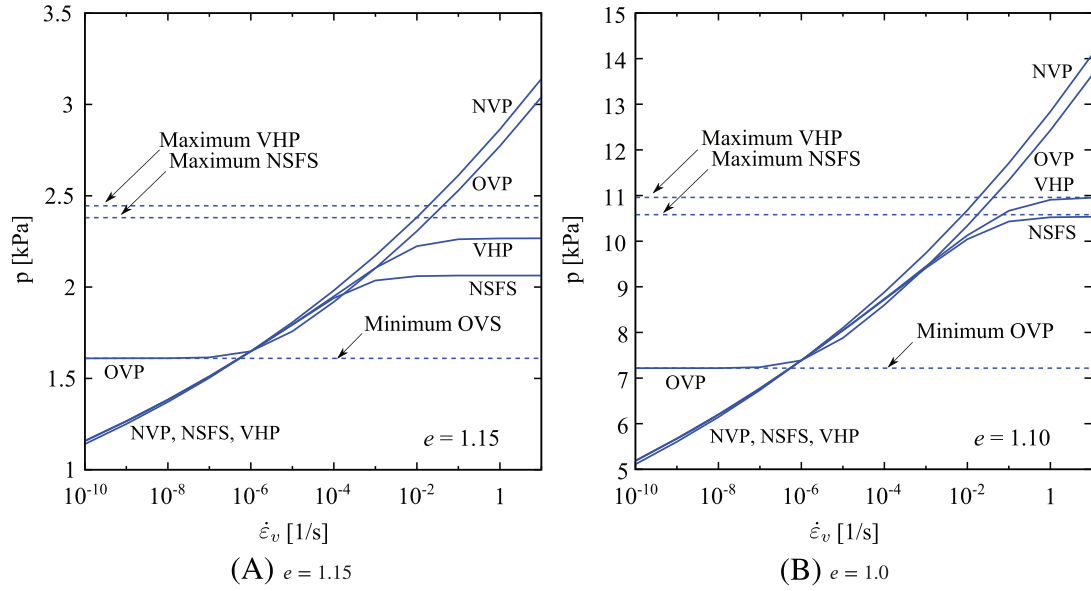


FIGURE 4 Mean pressure p at different rates $\dot{\epsilon}_v$ under isotropic compression

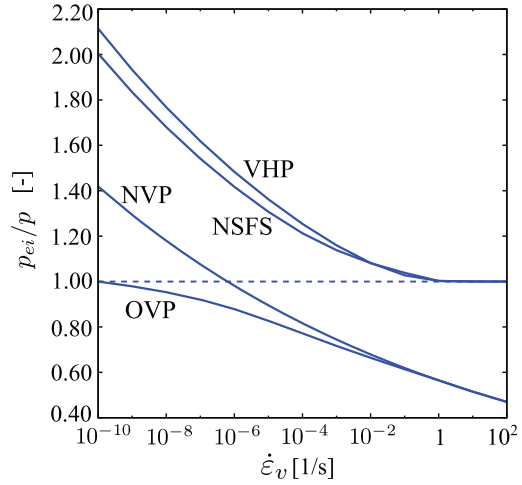


FIGURE 5 Stress ratio p_{ei}/p reached at different strain rates $\dot{\epsilon}_v$ upon isotropic compression

Similarly, the isotach condition for the VHP model is

$$\dot{p} = K(\dot{\epsilon}_v - \dot{\epsilon}_v^{\text{hp}} - \dot{\epsilon}_v^{\text{vis}}) = \frac{p(1+e)}{\lambda} \dot{\epsilon}_v. \quad (73)$$

Substitution of the corresponding definitions of K and $\dot{\epsilon}_v^{\text{hp}}$ in Equation (73) results in the following relation:

$$x\dot{\epsilon}_v = \dot{\epsilon}_v^{\text{vis}}, \quad \text{with } x = \frac{1 - Y_{0m}(p/p_{ei})^2}{1 - Y_{0m}}, \quad (\text{VHP model}). \quad (74)$$

Hence, two isotachs are related with the following relation for the VHP model:

$$\frac{\dot{\epsilon}_{v,a}}{\dot{\epsilon}_{v,b}} = \frac{\dot{\epsilon}_{v,a}^{\text{vis}}}{\dot{\epsilon}_{v,b}^{\text{vis}}} \frac{x_b}{x_a} = \left(\frac{\text{OCR}_b}{\text{OCR}_a} \right)^{1/l_v} \cdot \frac{x_b}{x_a}, \quad (\text{VHP model}). \quad (75)$$

The inequality $x_a \neq x_b$ is true considering that $x = x(p, e)$ is not a constant but rather a function of the mean stress p and void ratio e . Finally, we inspect the NSFS model. Considering the NSFS relations $x\dot{\epsilon}_v = \dot{\epsilon}_v^{\text{vis}}$, $\dot{\epsilon}_v^{\text{vis}} = \dot{\lambda}^{\text{vis}} = \dot{f}_t/A$, where

$A = (\partial F_e / \partial \sigma) : E : \mathbf{m} - \mathbf{1} : \mathbf{m} / C_p$, we write

$$\frac{x_a \dot{\epsilon}_{v,a}}{x_b \dot{\epsilon}_{v,b}} = \frac{\dot{\epsilon}_{v,a}^{\text{vis}}}{\dot{\epsilon}_{v,b}^{\text{vis}}} = \frac{\dot{f}_{t,a} / A_a}{\dot{f}_{t,b} / A_b}, \quad (\text{NSFS model}). \quad (76)$$

Substitution of $\dot{f}_t = I_v \lambda / C_p (1 / \text{OCR})^{1/I_v}$ in the latter equation gives

$$\frac{\dot{\epsilon}_{v,a}}{\dot{\epsilon}_{v,b}} = \left(\frac{\text{OCR}_b}{\text{OCR}_a} \right)^{1/I_v} \frac{A_b}{A_a} \frac{x_b}{x_a}, \quad (\text{NSFS model}). \quad (77)$$

One can show that for the NSFS model, the relation $x = (\kappa / \lambda - 1 + \lambda^{\text{pl}})$ holds. Equations (71), (72), (70), and (77) describe the isotach behavior for the NVP, OVP, VHP, and NSFS models, respectively. These equations relate two isotachs with each other and are functions of the void ratio e , mean pressure p , and volumetric strain rate $\dot{\epsilon}_v$. Their solutions coincide with the $e - p$ asymptotes reached by the compression curves at constant volumetric strain rates.

It should be emphasized that most existing one-dimensional isotache models tend to overestimate the creep strains measured after surcharge loading due to their viscous formulation $\varepsilon = 0.434 C_{\alpha\varepsilon} \ln(\dot{\epsilon}_1 / \dot{\epsilon})^{93}$ (with ε_1 being the axial strain). Yuan et al⁹³ proposed a two-parameter modification of this relation, which has resulted in a better match with laboratory data. Because of the potential dependence of the viscous strain rate on the overconsolidation ratio (see Equation 14), the creep settlements after surcharge loading may be predicted well by these models, as will be shown in Section 9.2. Furthermore, the viscous behavior of highly overconsolidated clays, ie, $\text{OCR} \geq 4$, is likely to be dominated by secondary swelling instead of creep. But certainly, the creep may resume after for example a decade-long wait.

9.2 | Creep test

Creep tests under isotropic states ($q = 0$) are now performed to evaluate the models response. The creep condition is simulated by restraining the effective stress for a large time, ie, $\dot{p} = 0$ and $q = 0$. Following Section 4, a similar response to the one described by the Buisman-type Equation 10 is expected from the simulations. For each model, two creep tests after isotropic compression were performed: Their initial conditions correspond to $e_0 = 1.2$, $p = 1$ kPa. An isotropic compression is applied but with distinct strain rates $\dot{\epsilon}_v = \{D_r, 5D_r\}$ for each test. In order to achieve the same creep response, D_r is chosen according to the values listed in Table 2, thus $D_r = 10^{-10}$ for OVP and $D_r = 10^{-6}$ for NSFS, NVP, and VHP. At the end, a creep path of 10^{10} seconds is performed.

Figures 6 and 7 present the simulations of all models. The response of the models can be summarized as follows: A similar slope of the creep test can be observed for all models in the e vs $\ln(t)$ space, see Figure 7, except by the OVP model. The slope is equal to C_α in the e vs $\ln(t)$ space, see Figure 7. The OVP model is the only one showing a lower bound for the creep deformation, because of the consideration of the minimum isotach. Of course, by choosing $\dot{\epsilon}_v^{\text{OVP}} = D_r^{\text{NSFS,NVP,VHP}}$, the creep behavior of OVP is more pronounced, and similar results to NVP are obtained.

The accurate simulation of creep is indispensable for predicting the flow pressure on dowelling elements of creeping slopes. The reduction of creep with OCR proves that the models can capture well the surcharge-induced stress history of the material. Hence, they may provide a realistic creep prediction and are able to control long-term settlements using surcharge loading.

Another, very important geotechnical issue in engineering practice is the prediction of long-term consolidation settlement, especially the process of residual settlement.⁹⁴⁻⁹⁶ In construction site, the consolidation settlement is generally estimated based on the $e - \ln(p_{ei})$ line obtained from a 24-hour incremental loading oedometer tests, which often corresponds to a strain rate of $\dot{\epsilon} = 10^{-7}$ /s. In order to achieve a more accurate prediction, Watabe and Leroueil⁹⁶ derived a relation for the creep strain using the compression index C_c at the consolidation pressure, the lower limit of the preconsolidation pressure, and the preconsolidation pressure at the respective strain rate. However, in situ strain rates are several orders smaller than those used in experiments. Considering Equation (11) in one dimension, which presents the basis for the multiaxial creep rate incorporated into the models, it can be concluded that one-dimensional compression creep can be captured well by the models as a function of in situ strain rate, C_α , C_c , and void ratio e .

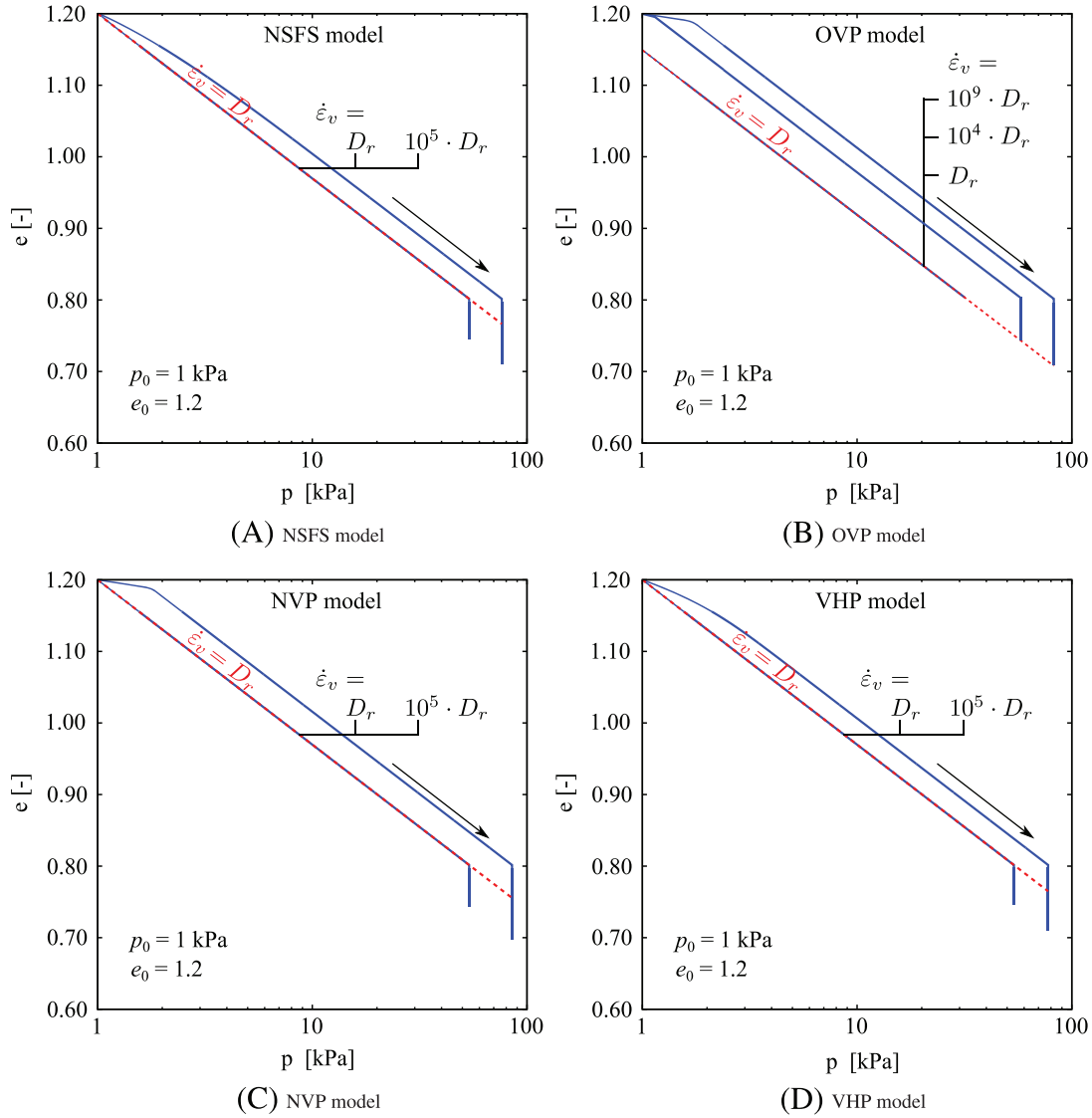


FIGURE 6 Creep tests after isotropic compression, e vs p space. D_r corresponds to the values listed in Table 2, thus $D_r = 10^{-10}$ for OVP and $D_r = 10^{-6}$ for NSFS, NVP, and VHP

9.3 | Stress relaxation test

Stress relaxation paths are now simulated under isotropic states ($q = 0$). The stress relaxation condition is achieved by restraining deformations under isotropic states, ie, $\dot{\epsilon} = \mathbf{0}$ with $q = 0$. Similar to the creep test, the stress relaxation is started after an isotropic compression path. For each model, two relaxation paths were simulated after isotropic compressions with strain rates of $\dot{\epsilon}_v = \{D_r, 5D_r\}$. In order to achieve a similar relaxation response, D_r is chosen according to the values listed in Table 2, thus $D_r = 10^{-10}$ for OVP and $D_r = 10^{-6}$ for NSFS, NVP, and VHP. Both relaxation paths start at different isotachs but with same void ratio $e = 0.8$. They simulate a period of $t = 10^{10}$ seconds. The results are plotted in Figures 8, 9, and 10.

Figure 9 shows that for a given void ratio, both simulations of each model yield asymptotically to the same curve in the p vs $\ln(t)$ space. The analytical solution of this asymptote is deduced later for all models except for the OVP model and is plotted with dashed lines in Figure 9A,C,D. Notice that the OVP model path is stopped by the minimum isotach, which acts as lower boundary. Of course, by choosing $\dot{\epsilon}_v^{\text{OVP}} = D_r^{\text{NSFS,NVP,VHP}}$, the relaxation behavior of OVP is more pronounced and similar results to NVP are obtained. In Figure 10, the curves are gathered together for comparison purposes.

We now proceed to deduce the analytical solution of the stress relaxation paths. Consider the NVP model constitutive Equation (42). The relaxation condition $\dot{\epsilon} = \mathbf{0}$, together with Equation (42) yields to $\dot{\epsilon} = \mathbf{E} : (-\dot{\epsilon}^{\text{vp}})$. Under isotropic

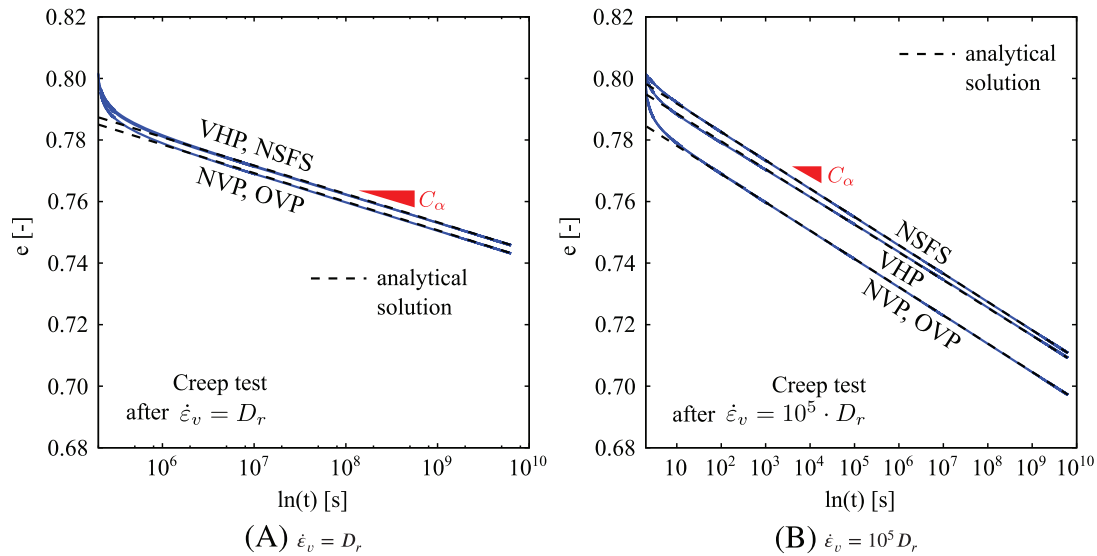


FIGURE 7 Creep tests after isotropic compression. Representation of the material parameters $C_\alpha = I_v/\lambda$. Analytical solution corresponds to Equation 10 and is solved for each constitutive equation. $D_r = 10^{-6}$ for both diagrams

stress conditions ($q = 0$), the latter relation is simplified to $\dot{p} = K (-\dot{\epsilon}_v^{\text{vp}})$. Substitution of $\dot{\epsilon}_v^{\text{vp}}$ (see Equation 43) and K (see Equation 24) yields to the relation

$$\dot{p} = \frac{p(1+e)}{\kappa} \left(-D_r \left(\frac{p}{p_{ei}} \right)^{1/I_v} \right), \quad (78)$$

which is an ordinary differential equation with solution $p = p(t)$. Let $c_{\text{nvp}} = c_{\text{nvp}}(e)$ denote the function of the void ratio $c_{\text{nvp}} = D_r (1+e) p_{ei}^{-1/I_v} / \kappa$. Substitution of c_{nvp} in Equation (78) leads to the simplified form

$$\dot{p} = -c_{\text{nvp}} p^{1+1/I_v} \quad \text{with solution} \quad p = \left(\frac{I_v}{c_{\text{nvp}} t - L_1} \right)^{I_v}, \quad (79)$$

where L_1 is an integration constant, for instance, found from the initial relaxation stress condition with $p(t=0) = p_0$:

$$L_1 = -\frac{I_v}{p_0^{1/I_v}} \quad (\text{integration constant solution for } p(t=0) = p_0). \quad (80)$$

Substituting L_1 into Equation (79) yields to the relation

$$p = \left(\frac{I_v c_{\text{nvp}}}{t + I_v / (c_{\text{nvp}} p_0^{1/I_v})} \right)^{I_v} = \left(p_0^{-1/I_v} + \frac{c_{\text{nvp}}}{I_v} t \right)^{-I_v} \quad (\text{NVP}). \quad (81)$$

A similar mathematical procedure can be followed to find the analytical solutions for the NSFS and VHP models. Consider the constitutive Equations (22) and (46) under the conditions $q = 0$ and $\dot{\epsilon} = 0$:

$$\dot{p} = \frac{p(1+e)}{\kappa} (-\dot{\epsilon}_v^{\text{vp}}), \quad \dot{\epsilon}_v^{\text{vp}} = \dot{\lambda} = \frac{I_v \lambda \kappa}{\lambda - \kappa} \left(\frac{p}{p_{ei}} \right)^{1/I_v} \quad (\text{NSFS}), \quad (82)$$

$$\dot{p} = \frac{p(\lambda + \kappa)(1+e)}{2\lambda\kappa} (-\dot{\epsilon}_v^{\text{vp}}), \quad \dot{\epsilon}_v^{\text{vp}} = I_v \lambda \left(\frac{p}{p_{ei}} \right)^{1/I_v} \quad (\text{VHP}). \quad (83)$$

One may show that the same differential Equation (79) is obtained if replacing the constant c_{nvp} by the function $c_{\text{nsfs}} = c_{\text{nsfs}}(e) = I_v \lambda (1+e) p_{ei}^{-1/I_v} / (\lambda - \kappa)$ for the NSFS model and by $c_{\text{vhp}} = c_{\text{vhp}}(e) = I_v (\lambda + \kappa) (1+e) p_{ei}^{-1/I_v} / (2\kappa)$ for the

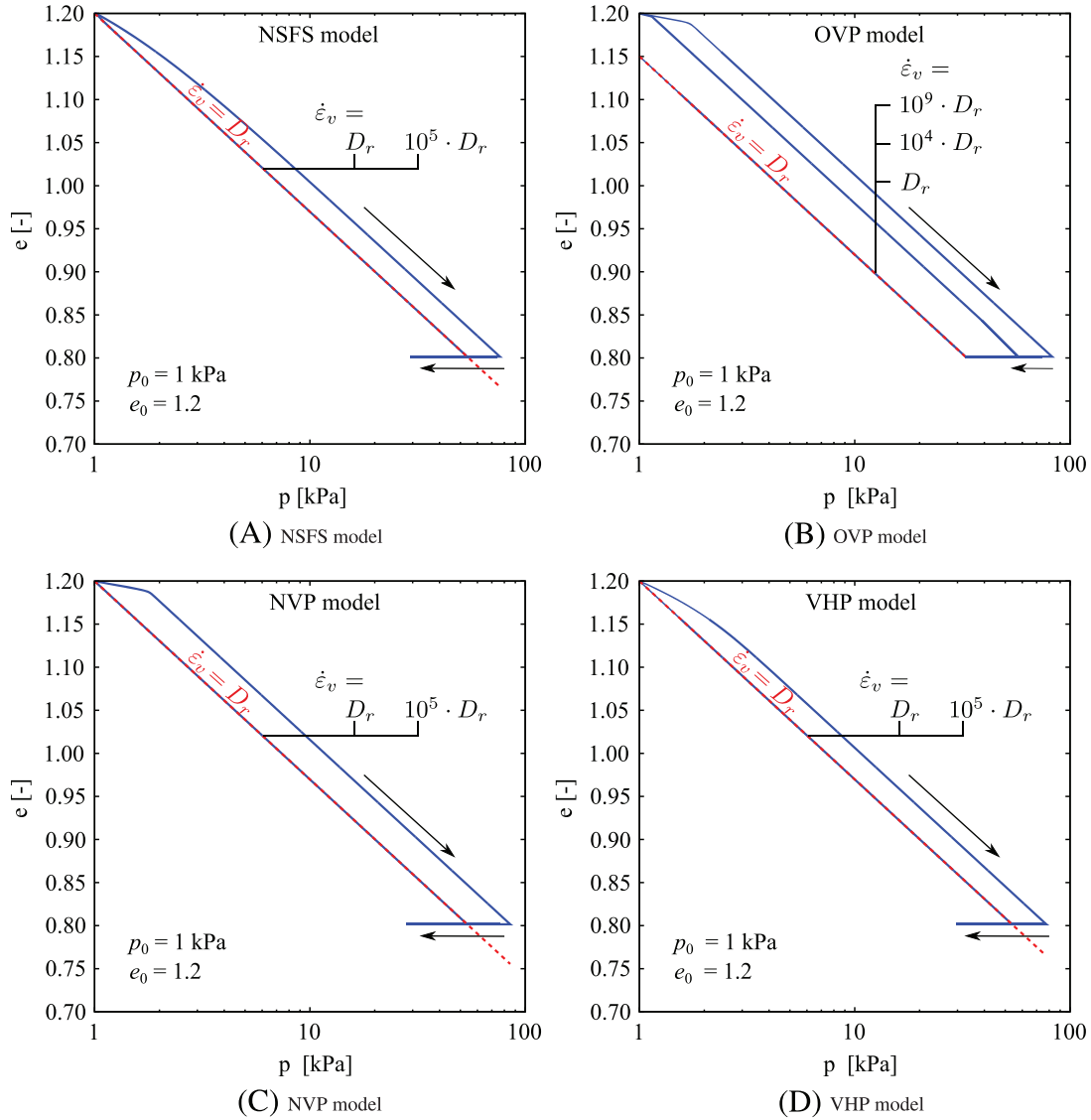


FIGURE 8 Stress relaxation tests after isotropic compression. D_r corresponds to the values listed in Table 2, thus $D_r = 10^{-10}$ for OVP and $D_r = 10^{-6}$ for NSFS, NVP, and VHP

VHP model. Following the same procedure, one can show that the simplified differential form describing the relaxation process ($q = 0$, $\dot{\epsilon} = \mathbf{0}$) of the OVP model is

$$\dot{p} = -c_{\text{ovp}} \left(p^{1+1/I_v} + p p_{e,\min}^{1/I_v} \right) \quad (\text{OVP}), \quad (84)$$

whereby $c_{\text{ovp}} = D_r (1+e) p_{ei}^{-1/I_v} / \kappa$ is a void ratio function. The latter equation lacks of analytical solution. Figure 9 includes the analytical solutions of the NSFS, NVP, and VHP models.

9.4 | Response envelopes

Response envelopes were originally proposed by Gudehus⁹⁷ to analyze the directional response of constitutive models. The shape of response envelopes in the p - q space results from joining the end points of different p - q paths, all of them beginning with the same initial conditions ($e = e_0$, $\sigma = \sigma_0$) and subjected to identical strain increment magnitude $\|\Delta\epsilon\| = 0.2\%$ on different strain rate directions $\vec{\epsilon}$. The analysis is usually performed under triaxial conditions.

For each model, four different response envelopes are constructed under triaxial conditions. Two initial conditions were considered: at isotropic stress states, with $p = 100$ kPa, $q = 0$, and at anisotropic stress states at $p = 100$ kPa and $q = 75$

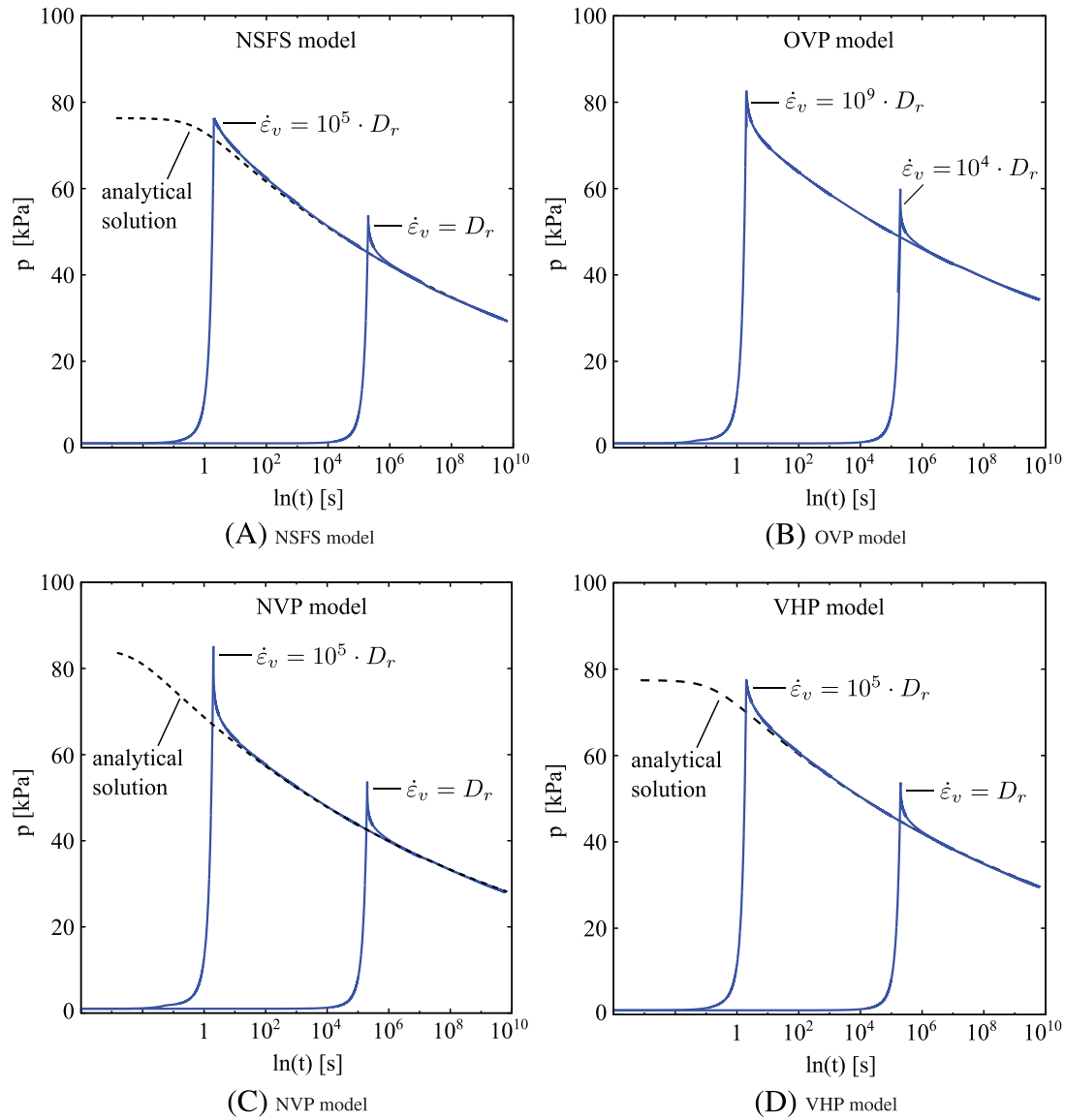


FIGURE 9 Stress relaxation tests after isotropic compression. Analytical solution according to Equation 81, with the respective void ratio functions c_{nsfs} , c_{nvp} , and $c_{\text{vhp}} \cdot D_r$ corresponds to the values listed in Table 2, thus $D_r = 10^{-10}$ for OVP and $D_r = 10^{-6}$ for NSFS, NVP, and VHP

kPa. For each initial state, two different strain velocities were applied, $\|\dot{\epsilon}\| = 10^{-5}$ 1/s and $\|\dot{\epsilon}\| = 10^{-7}$ 1/s. The results are plotted in Figure 11. From the results, the following observations are commented:

- Response envelopes showed larger stress increments $\Delta\sigma$ for the lowest strain rate case ($\|\dot{\epsilon}\| = 10^{-7}$ 1/s). They showed also that the effect of the strain rate is only evident in a particular zone of the response envelope. The zone showing no strain rate dependency is governed by the elastic response of the model.
- The NSFS and VHP models showed lower strain-rate dependency than other models. This is related to the fact that both models incorporate the maximum isotach and the selected initial conditions are close to the maximum isotach. Therefore, their viscous effects are in some way bounded.
- In contrast to other models, response envelopes of the NSFS model present corners at points dividing the elastic and viscoplastic response. Other models showed rounded shape. Corners on responses envelopes are typical on elastoplastic formulations and coincide with the division of the elastic and (visco-)plastic response.⁵⁵ To the date, these corners have not been experimentally found.
- The response envelope of the VHP model with initial conditions of $p = 100$ kPa and $q = 75$ kPa shows a “rotation” of its main axis with slope similar to the critical state. Other models do not show this “rotation.” This rotation is attributed

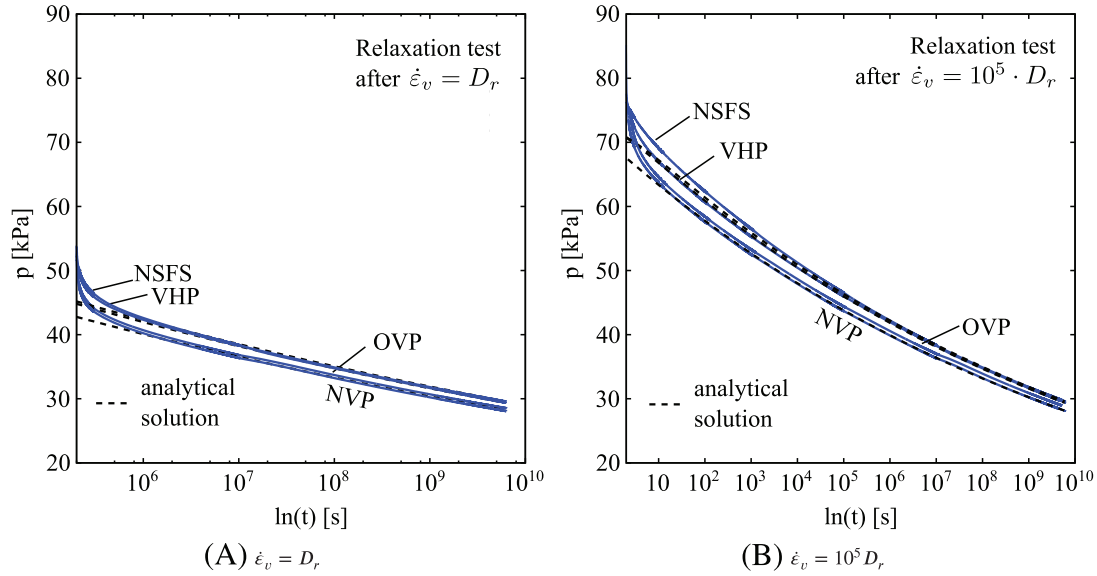


FIGURE 10 Stress relaxation tests after isotropic compression. Analytical solution according to Equation 81, with the respective void ratio functions c_{nsfs} , c_{nvp} , and c_{vhp} . $D_r = 10^{-6}$ for both diagrams

to the formulation of the (hypo-)elastic stiffness, which, for this model, incorporates the dilatant terms $\mathbf{E} \sim (\mathbf{1r} + \mathbf{r1})$. Rotated responses envelopes have been already observed in experimental works.^{98,99}

9.5 | Simulation of undrained triaxial creep tests

Undrained creep has been observed in many experimental works with soft soils,¹⁰⁰⁻¹⁰⁴ and its simulation has been addressed in other works.^{38,39,44,50,59,105} The usual procedure is to perform an undrained triaxial test until a small value of axial strain is reached. Thereafter, the axial stress σ_1 and confining pressure σ_3 are kept constant. In terms of Roscoe invariants q and p , the deviator stress is kept constant $\dot{q} = 0$, while the mean (effective) stress p is allowed for variations. These conditions result in a creep process leading to the development of pore pressures p_w and axial strains ϵ_1 under undrained conditions ($\dot{\epsilon}_v = 0$). Details of undrained creep can be found in other works.¹⁰⁶⁻¹⁰⁹ Under the mentioned conditions, an acceleration of the creep process is sometimes evident when the deviator stress is close to the maximum deviator stress q_f , ie, $q \approx q_f$. This creep acceleration has been referred to as “tertiary creep” by some authors.^{107,110,111} Eventually, a pronounced acceleration of the axial strains may lead to the failure of the sample and loss of controllability. This case is known as “undrained creep rupture” and has been also studied in other works. In the following lines, we examine the capabilities of the different models with respect to these observations.

Undrained creep is simulated with the four models. Initial conditions under isotropic states $q = 0$ were assigned to match a void ratio $e = 0.739$ and mean stress of $p = 100$ kPa. These initial conditions coincide with a point at the reference isotach, ie, $R_{\text{ref}} = 1$. An undrained shearing under triaxial conditions is then performed with a strain velocity of $\|\dot{\epsilon}\| = 10D_r$. The undrained shearing is stopped at different axial strain levels ϵ_1 . Subsequently, undrained creep ($q = 0$) is simulated for a period of 10^6 seconds. Figures 12 and 13 present the simulations in the q vs ϵ_1 space and p vs q space. A monotonic undrained test with the same strain velocity has been also included for comparison purposes. Four different creep paths were simulated, each at different q . Simulations show that all models are able to simulate undrained creep, which is obvious because of their formulations. The resulting strain velocity under the undrained creep is examined in Figure 14. The only models evidencing simulations of tertiary creep, ie, a strain acceleration, correspond to the NSFS and VHP models; see Figure 14A,D. Figure 14D shows that these special cases ended with creep rupture because the condition $\dot{\epsilon}_s \rightarrow \infty$ is reached. Other models did not show evidence of this capability. According to Vermeer and Neher,⁵⁹ a NVP-type model can also reproduce tertiary creep, when the viscous strain is formulated as follows:

$$\dot{\epsilon}^{\text{vp}} = \frac{1}{\alpha} D_r \left(\frac{1}{\text{OCR}_{3\text{D}}} \right)^{1/I_v} \mathbf{m}, \quad \text{with} \quad \alpha = \frac{\partial f}{\partial p} = 1 - \left(\frac{q}{M p} \right)^2. \quad (85)$$

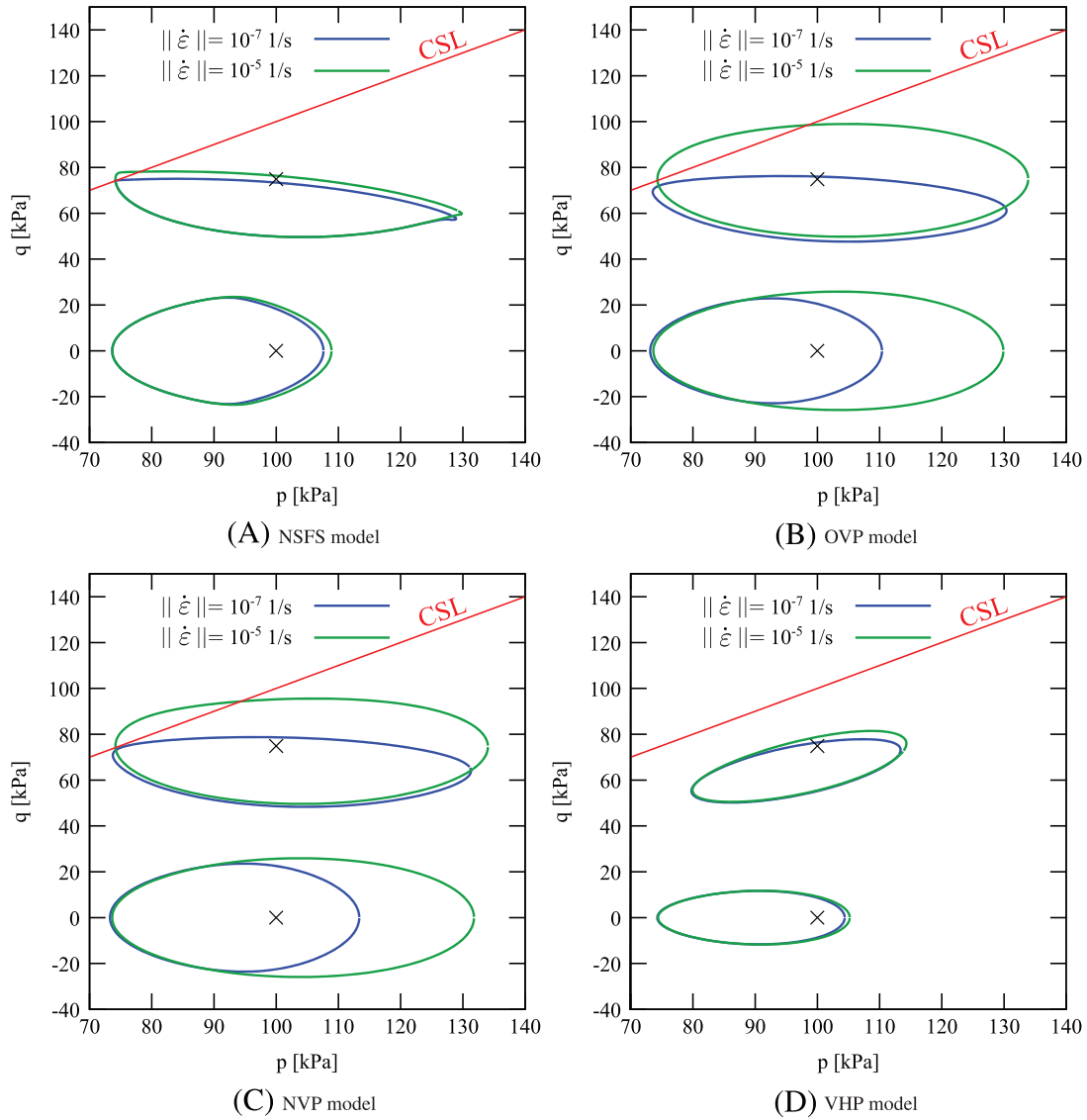


FIGURE 11 Response envelopes constructed at different initial conditions ($p = 100$ kPa, $q = 0$) and ($p = 100$ kPa and $q = 75$ kPa) and different strain rates ($\|\dot{\epsilon}\| = 10^{-5}$ 1/s and $\|\dot{\epsilon}\| = 10^{-7}$ 1/s)

Note that α is a function of the stress and tends to $\alpha \rightarrow \infty$ for states very close to critical states. Some simulation examples with this modification are shown in Figure 13 in $p-q$ and $q-\varepsilon_1$ plane, and in Figure 14(E), the strain acceleration leading to creep rupture is presented.

We now examine the creep rupture condition under undrained triaxial tests for the models NSFS and VHP. Consider triaxial conditions, such that one may simplify the constitutive Equations (46) and (28) to

$$\begin{pmatrix} \dot{p} \\ \dot{q} \end{pmatrix} = \begin{pmatrix} K_{11} & K_{12} \\ K_{21} & K_{22} \end{pmatrix} \begin{pmatrix} \dot{\varepsilon}_v \\ \dot{\varepsilon}_s \end{pmatrix} + \begin{pmatrix} \dot{p}^{\text{vis}} \\ \dot{q}^{\text{vis}} \end{pmatrix} \quad (86)$$

where $\dot{p} = -(\dot{\sigma}_{11} + 2\dot{\sigma}_{22})/2$, $\dot{q} = -(\dot{\sigma}_{11} - \dot{\sigma}_{22})$, $\dot{\varepsilon}_v = -(\dot{\varepsilon}_{11} + 2\dot{\varepsilon}_{22})$ and $\dot{\varepsilon}_s = -2/3(\dot{\varepsilon}_{11} - \dot{\varepsilon}_{22})$ are the rates of the Roscoe invariants, \dot{p}^{vis} and \dot{q}^{vis} are the Roscoe invariants of $\dot{\boldsymbol{\sigma}}^{\text{vis}}$, and K_{ij} are the resulting stiffness coefficients. Imposition of the undrained creep conditions $\dot{q} = 0$ and $\dot{\varepsilon}_v = 0$ in Equation (86), leads to the following relation:

$$0 = K_{22}\dot{\varepsilon}_s + \dot{q}^{\text{vis}} \quad (\text{undrained creep}). \quad (87)$$

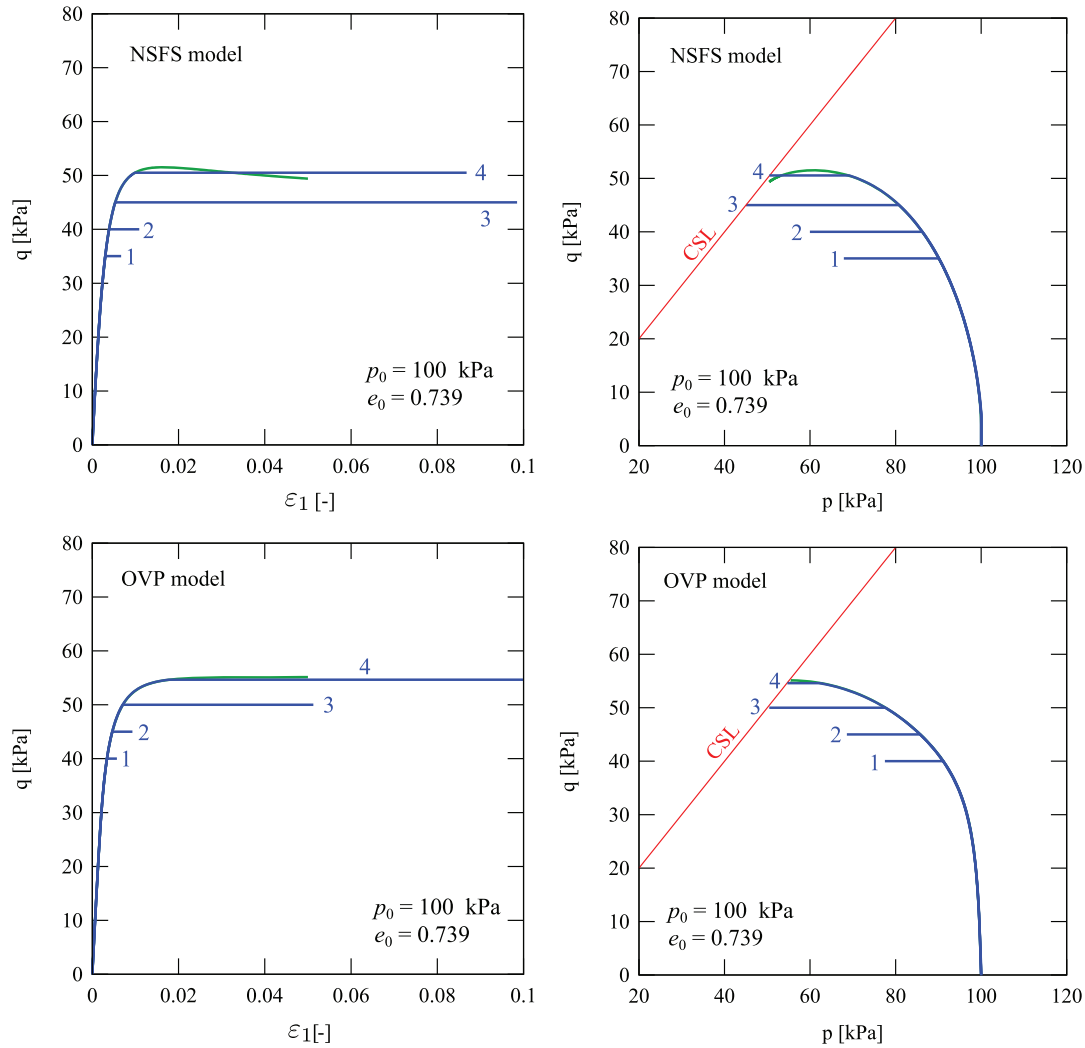


FIGURE 12 Simulations of undrained creep at different deviator stresses q with NSFS and OVP

The creep rupture is experienced when $\dot{\epsilon}_s \rightarrow \infty$ or equivalently

$$K_{22} = 0 \quad (\text{undrained creep rupture condition}). \quad (88)$$

Computation of the scalar function K_{22} is not an easy task. It depends on the mean stress p , the deviator stress q , and the void ratio e . For the case of the NSFS model, it also depends on the state variable ϵ_v^{VP} , which makes its solution path dependent. Hence, we find a solution only for the VHP model. For a given void ratio e , one may numerically solve a set of points $p - q$ solving the condition $K_{22} = 0$. For this purpose, a special script in the software WOLFRAM MATHEMATICA has been implemented. Some details of the programming lines are given in Appendix C. Figure 14(F) shows some envelopes of the creep rupture condition $K_{22} = 0$ for the VHP model. Three different solutions are found for different void ratios $e = \{0.7, 0.75, 0.8\}$. The surface described by the condition $\text{OCR}_{3D} = 1$, see Equation 8, is also included for comparison purposes. Notice that for a given void ratio, the rupture curve is found to the right side of the CSL line at high deviator stresses q . This is in accordance with simulations and also experimental observations.

Now, we will compare the simulated response of undrained triaxial creep tests (UTCTs) of Haney clay with test data provided by Vaid and Campanella.¹¹² The material parameters are listed in Figure 2. All samples have been initially consolidated to $p = 525$ kPa for a period of time required to reach $p_{ei} = 373$ kPa. Subsequently, undrained creep tests were performed at constant deviatoric stresses of $q = \{278.3, 300.3, 323.4\}$ kPa. Creep under constant shear stress is observed at for all three values of q . All models are able to describe this behavior in accordance with the experimental evidence as shown in Figure 15. The OVP model shows that it can not capture the undrained creep for $q = 278.3$ kPa $\Rightarrow q/q_{\max} = 75\%$.

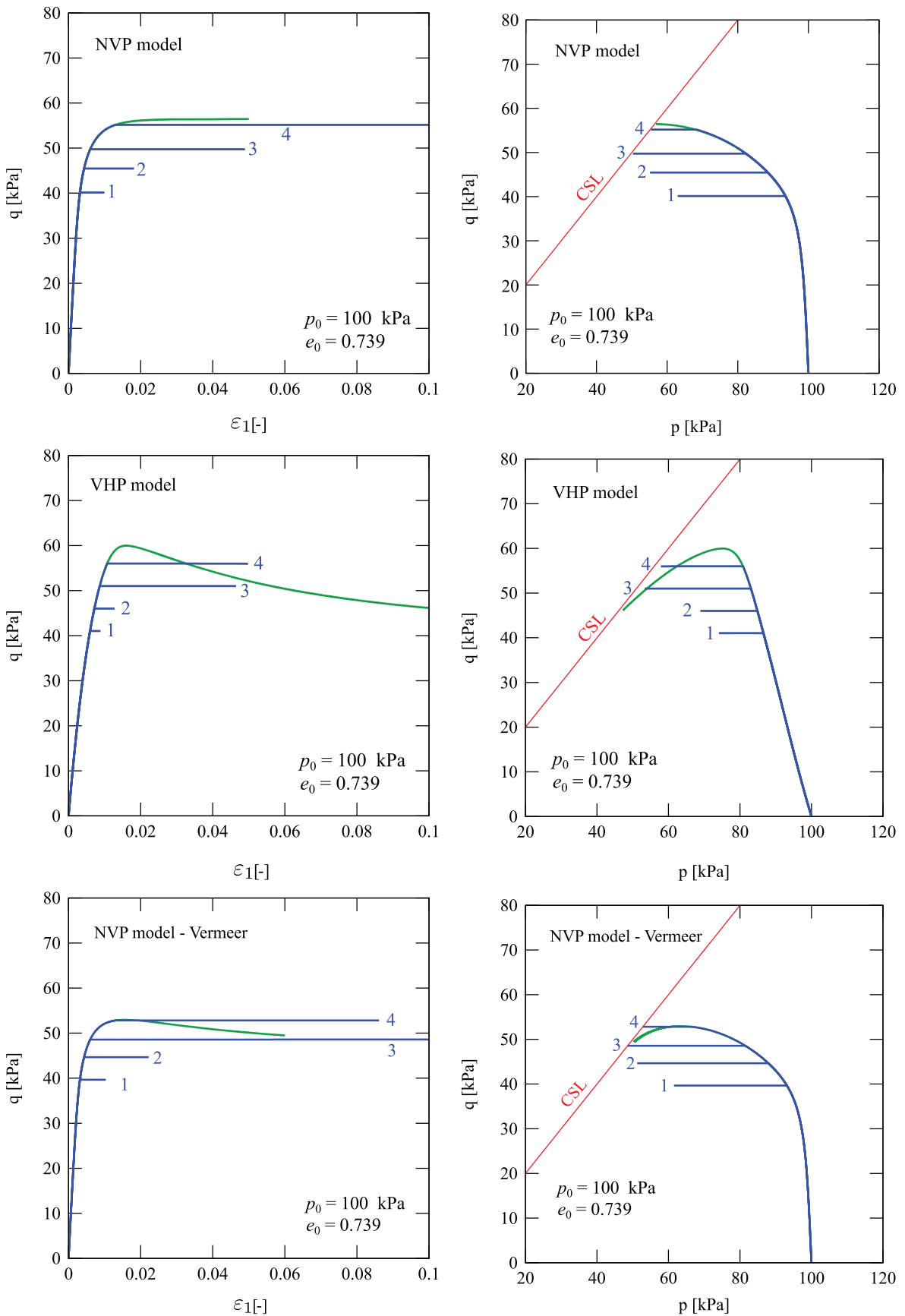


FIGURE 13 Simulations of undrained creep at different deviator stresses q with NVP, VHP, and NVP after Vermeer and Neher⁵⁹

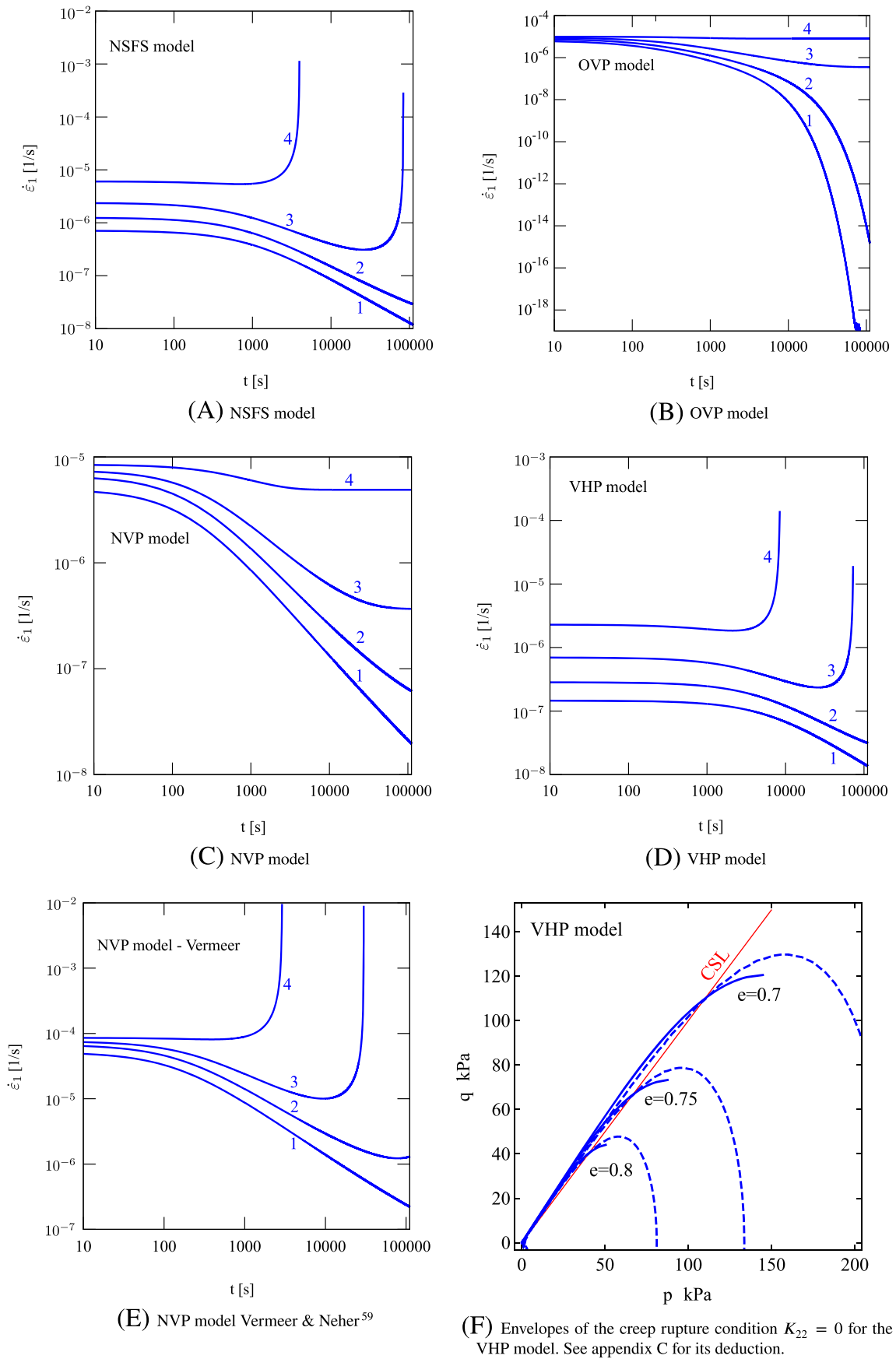


FIGURE 14 Plots of axial strain rates $\dot{\epsilon}_1$ against time t during undrained creep, see Figures 12 and 13

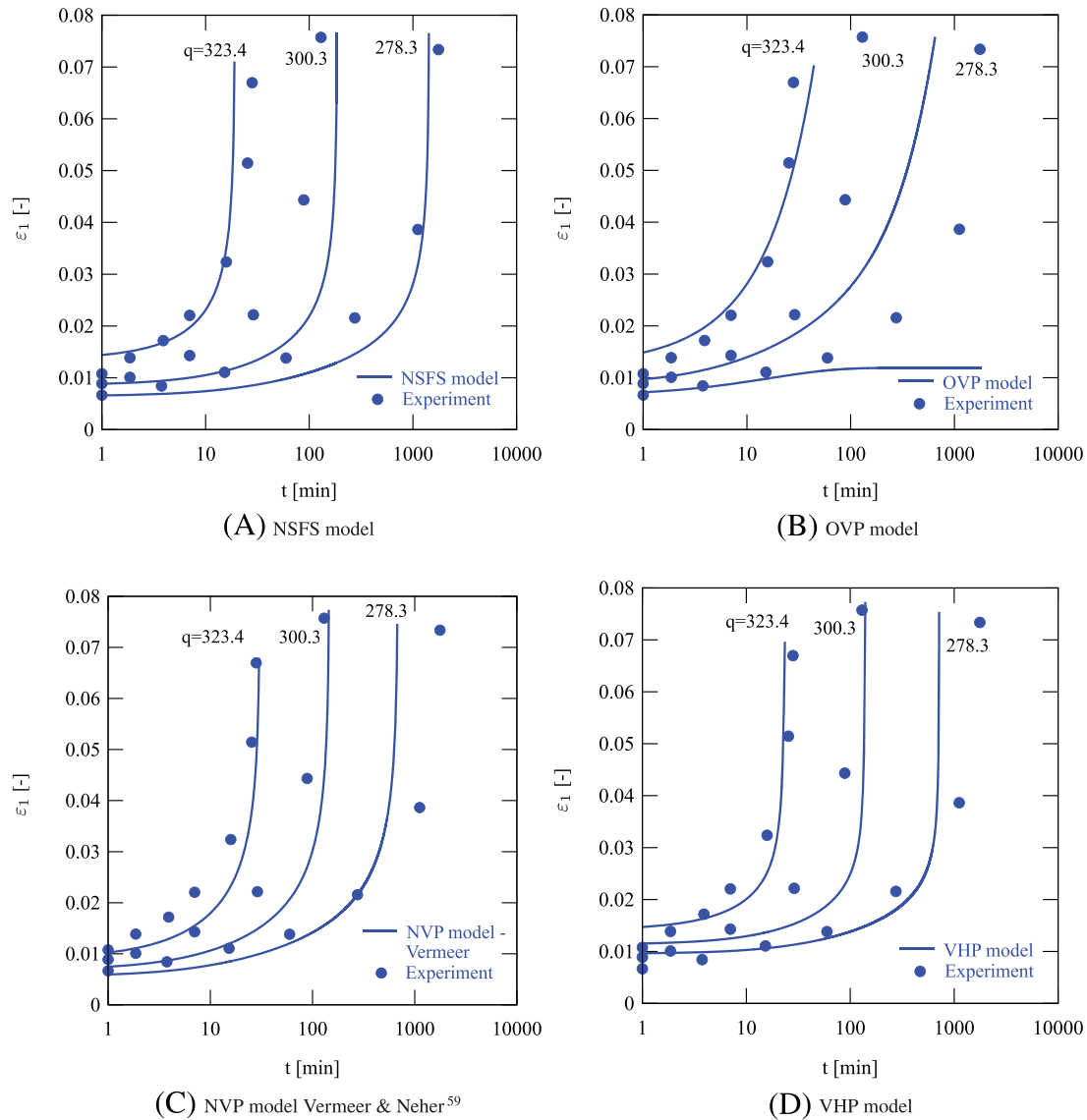


FIGURE 15 Results of triaxial creep tests. Normally consolidated samples with $p_0 = 700$ kPa were sheared to different deviatoric stresses $q = \{278.3, 300.3, 323.4\}$ kPa. Subsequently, undrained creep under constant q is observed

By shifting the reference isotach, one could achieve undrained creep for $q = 278.3$ kPa as well, but then the simulations for $q = \{300.3, 323.4\}$ kPa would greatly overestimate the undrained creep rendered by the experiments. From Figure 15, it is also evident that all models, except for OVP, reach a vertical tangent. Hence, NSFS, NVP, and the VHP models are able to simulate tertiary creep in accordance with experimental results and the aforescribed qualitative simulations. At this point, it is worthy to note that the flow rule term α , introduced in Equation (85), could also be applied to an overstress-type model, making OVP models capable of capturing tertiary creep.

The accurate simulation of these effects are of great importance for the assessment of the failure probability of a creeping slope due to accelerated (tertiary) creep. Creep in general is indispensable for predicting the flow pressure on dowelling elements of these slopes.

9.6 | Simulation of an oedometric test with different strain rates

The assessment of the models is now examined with simulations of an experimental study. The tested material corresponds to a Kaolin clay reported by Niemunis and Krieg.⁷ The Kaolin is a medium plasticity clay with plasticity index equal to $PI = 12, 2\%$. Reconstituted samples of height and diameter equal to 50 mm were used for this purpose. The experiment consists of a volumetric compression under oedometric conditions considering strain rate effects and unloading-reloading

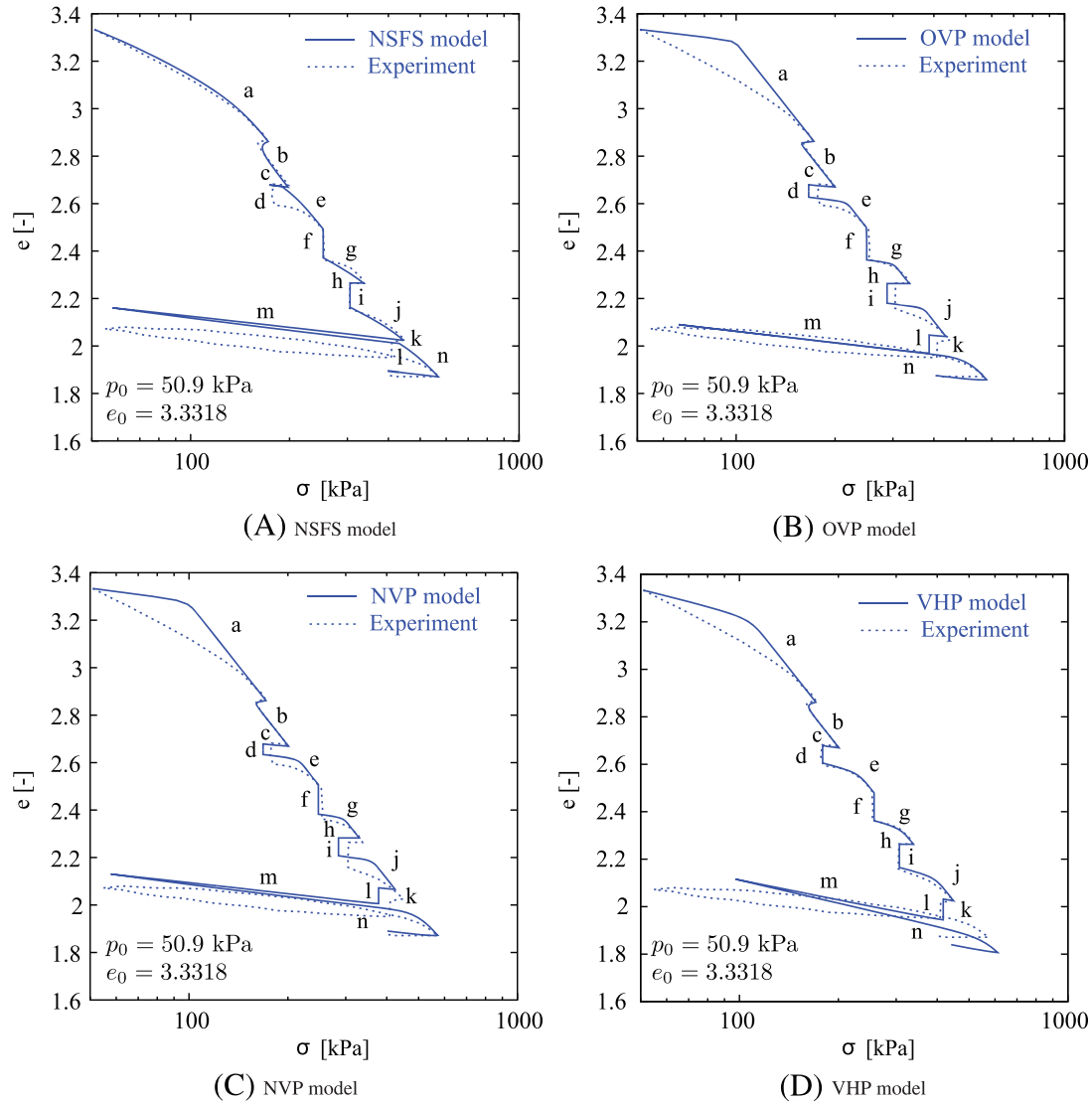


FIGURE 16 Oedometer test with loading, unloading-reloading, relaxation, and creep stages. Experiment on a Kaolin clay reported by⁷ with the axial strain rate $\dot{\epsilon}_1$ corresponding to $a = 0.936 \text{ \%/h}$, $b = e = g = j = n = 0.156 \text{ \%/h}$, $c = k = -0.0156 \text{ \%/h}$, $m = -0.156 \text{ \%/h}$, one relaxation phase h and four creep stages d, f, i, l

Model	1	2	3	4	5	6	7
NSFS model		x	x			x	x
OVP model	x	x			x		
NVP model							x
VHP model		x					

TABLE 4 Some properties shown by the simulations of the different models

Note. 1: limited creep deformation; 2: limited stress relaxation; 3: maximum isotach for very high strain rates; 4: loss of convexity and corners on responses envelopes; 5: absence of undrained creep rupture; 6: absence of instant creep after unloading path; 7: ability to simulate viscous and nonviscous materials.

cycles. The experimental path includes creep and relaxation stages. The calibrated parameters are listed in Table 2, and the characteristic void ratios e_{i0} describing the OCR= 1 isotach in Table 3. In Figure 16, dashed lines represent the experimental curve, while continuous lines represent the simulations.

The simulations showed some relevant aspects of the model capabilities: All models, except by the NSFS model, were able to reproduce creep after an unloading path. The sequence loading-unloading-creep forced the NSFS model to remain under elastic response and thus to present at that instance a complete inability to simulate creep. This implies that, for the NSFS, an infinitesimal unloading disables the creep simulation. This is of course against experimental observations and may be considered as one of the main disadvantages of classical NSFS models. Other strain-rate dependencies were satisfactory captured by all models.

10 | DISCUSSION AND FINAL REMARKS

The present work was devoted to review four different models for viscous clays belonging to different model families, namely, NSFS, NVP, OVP, and VHP. In order to perform a fair comparison, the developed formulations accounted for the same material parameter definitions, same reference isotach, and other rules established in Section 5. Numerical investigations allowed to detect a number of discrepancies related to their formulations. Some of them are in the following lines mentioned, while others were directly within the text indicated: Discrepancies observed at simulations of creep and stress relaxation are mostly related to the consideration of a maximum and/or minimum isotach in their formulations. While the OVP model incorporates a minimum isotach, at which no more rate effects are experienced for creep and stress relaxation, the NSFS and VHP model present a maximum isotach, which bounds instant time effects. The NVP model does not incorporate any of these bounding isotachs. Response envelopes showed that viscous effects are exhibited only at certain stress rate directions by all models, and a loss of convexity in conjunction with the appearance of corners were only noticed on those from the NSFS model. The undrained creep analysis showed that models having a strain rate with three components, such as the NSFS and VHP, are prone to include the simulation of undrained creep rupture in their capabilities. The simulation of a real oedometer test, including strain-rate dependencies, showed that the NSFS model can not simulate creep after an unloading path. Finally, it seems that the consideration of a maximum isotach allows the formulation to enable the simulation of viscous and nonviscous clays. The latter point was not illustrated through simulations but shown directly through their formulations. Table 4 provides a summary of these observations. As a final note, it is recalled that the observations listed in Table 4 hold only for the formulations inspected herein, which were proposed according to their original works for each model family. The consideration of a Buisman-type relation for the description of creep processes leads to an accurate estimation of the viscous behavior such as for example the prediction of creep settlements after surcharge loading. Creep in general is indispensable for predicting the flow pressure on dowelling elements of creeping slopes. All models can be used for this purpose. The accurate simulation of tertiary creep is of great importance for the assessment of the failure probability of these slopes due to accelerated (tertiary) creep. The NSFS, VHP, and NVP (with the extension proposed in Vermeer and Neher⁵⁹) models have shown the ability to describe these effects well. Furthermore, it can be concluded that the simulation of tertiary creep can be achieved by different assumptions ie, using three components models (elastic+plastic+viscoplastic) or a modified flow rule (with $\alpha \rightarrow \infty$ for states close to critical states).

Of course, special extensions of the studied models may provide different features and therefore different conclusions but were not studied to keep simplicity.

REFERENCES

1. Graham J, Crooks JHA, Bell AL. Time effects on the stress-strain behaviour of natural soft clays. *Géotechnique*. 1983;33(3):327-340.
2. Nash DFT, Sills GC, Davison LR. One-dimensional consolidation testing of soft clay from Bothkennar. *Géotechnique*. 1992;42(2):241-256.
3. Hight DW, Bond AJ, Legge JD. Characterization of the Bothkennar clay: an overview. *Géotechnique*. 1992;42(2):303-347.
4. Nash DFT, Powell JJM, Lloyd IM. Initial investigations of the soft clay test site at Bothkennar. *Géotechnique*. 1992;42(2):163-181.
5. Jardine RJ, Lehane BM, Smith PR, Gildea PA. Vertical loading experiments on rigid pad foundations at Bothkennar. *Géotechnique*. 1995;45(4):573-597.
6. Krieg S. Viskoses Bodenverhalten von Mudden, Seeton und Klei. PhD Dissertation. Institut für Boden- und Felsmechanik der Universität Karlsruhe Germany Heft 150 2000.
7. Niemunis A, Krieg S. Viscous behaviour of soils under oedometric conditions. *Can Geotech J*. 1996;33(1):159-168.
8. Sivakumar V, Jeludine DKNM, Bell A, Glynn DT, Mackinnon P. The pressure distribution along stone columns in soft clay under consolidation and foundation loading. *Géotechnique*. 2011;61(7):613-620. TECHNICAL NOTE.
9. Della VG, Romero E. A fully coupled elasticplastic hydromechanical model for compacted soils accounting for clay activity. *Int J Numer Anal Methods Geomech*. 2013;37:503-535.

10. Kamal RH, Coop MR, Jardine RJ, Brosse A. The post-yield behaviour of four Eocene-to-Jurassic UK stiff clays. *Géotechnique*. 2014;64(8):620-634.
11. Tan F, Zhou W, Yuen K. Effect of loading duration on uncertainty in creep analysis of clay. *Int J Numer Anal Methods Geomech*. 2018; 42(11):1235-1254. <https://doi.org/10.1002/nag.2788>
12. Ng CWW, Liu GB, Lia Q. Investigation of the long-term tunnel settlement mechanisms of the first metro line in Shanghai. *Can Geotech J*. 2013;50(6):674-684.
13. Rezanian M, Taiebat M, Poletti E. A viscoplastic SANICLAY model for natural soft soils. *Comput Geotech*. 2016;73:128-141.
14. Sexton BG, McCabe BA, Karstunen M, Sivasithamparan N. Stone column settlement performance in structured anisotropic clays: the influence of creep. *J Rock Mech Geotech Eng*. 2016;8(5):672-688.
15. Yang C, Carter J. 1-D finite strain consolidation analysis based on isotach plasticity: Class A and Class C predictions of the Ballina embankment. *Comput Geotech*. 2018;93:42-60.
16. Black JA, Sivakumar V, Bell A. The settlement performance of stone column foundations. *Géotechnique*. 2011;61(11):909-922.
17. Killeen MM, McCabe BA. Settlement performance of pad footings on soft clay supported by stone columns: a numerical study. *Soils Found*. 2014;54(4):760-776.
18. Buehler MM, Cudmani R, Gudehus G. Experimental and numerical investigation of the behaviour of piles in soft soils under monotonic and alternating loading. In: *The 13th World Conference on Earthquake Engineering, Vancouver, BC, Canada, Paper*; 2004:431-438.
19. Leroueil S. Natural slopes and cuts: movement and failure mechanisms. *Géotechnique*. 2001;51(3):197-243.
20. Mahajan SP, Muniram B. Viscous effects on penetrating shafts in clays. *Acta Geotechnica*. 2006;1(3):157-165.
21. Mahajan SP, Budhu M. Shear viscosity of clays using the fall cone test. *Géotechnique*. 2009;59(6):539-543. TECHNICAL NOTE.
22. Selvadurai APS. The time-dependent response of a deep rigid anchor in a viscoelastic medium. *Int J Rock Mech Mining Sci Geomech Abstracts*. 1978;15(1):11-19. Pergamon Press printed in Great Britain.
23. Bundred J. On-site measurements of earth pressure and anchor forces for a diaphragm retaining wall. In: *Proceedings of symposium on field instrumentation in geotechnical engineering London*. London: British Geotechnical Society; 1973:52-69.
24. Liu TK, Dugan JP. An instrumented tied back deep excavation. *Performance of Earth and Earth Supported Structures*. 1972;1(2):1323-1339. Purdue.
25. Haws ET, Lippard DC, Tabb R, Burland JB. Instrumentation for the National Westminster Bank Tower. In: :180-193; 1973. British Geotechnical Society, London.
26. Hanna TN. *Foundations in Tension—Ground Anchors*. New York: Trans. Tech. Publication and McGraw-Hill Book Co.; 1982:563.
27. Buisman K. Results of long duration settlement test. In: no. 1:103-107; 1936; Cambridge, MA.
28. Taylor DW. *Research on consolidation of clays*. Cambridge, MA: Massachusetts Institute of Technology. 1942;(Series 82).
29. Taylor D. *Fundamental of soil mechanics*. 66 New York: Wiley; 1948:161.
30. Suklje L. *Rheological Aspects of Soil Mechanics*. Jhon Wiley and Sons-Interscience; 1969.
31. Singh A, Mitchell JK. General stress-strain-time function for soils. *J Soil Mech Found Div ASCE*. 1968;94(1):21-46.
32. Mesri G. Coefficient of secondary compression. *J Soil Mech Found Div ASCE*. 1973;99(1):123-137.
33. Yin JH. Non-linear creep of soils in oedometer tests. *Géotechnique*. 1999;49(5):699-707. TECHNICAL NOTE.
34. Schofield A, Wroth P. *Critical State Soil Mechanics*. London: Mc Graw Hill; 1968.
35. Borja RI, Seung RL. Cam clay plasticity, part 1: Implicit integration of elasto-plastic constitutive relations. *Comput Methods Appl Mech Eng*. 1990;78(1):49-72.
36. Borja RI. Generalized creep and stress relaxation model for clays. *J Geotech Eng Div ASCE*. 1992;118(11):1765-1786.
37. Yao YP, Kong LM, Hu J. An elastic-viscous-plastic model for overconsolidated clays. *Sci China Technol Sci*. 2013;56(2):441-457.
38. Sekiguchi H. Theory of undrained creep rupture of normally consolidated clay based on elasto-viscoplasticity. *Soils Found*. 1984;24(1):129-147.
39. Hashiguchi K, Okayasu T. Time-dependent elastoplastic constitutive equation based on the subloading surface model and its application to soils. *Soils Found*. 2000;40(4):19-36.
40. De GV, Pereira JM. A viscoplastic constitutive model for unsaturated geomaterials. *Comput Geotech*. 2013;54:143-151.
41. Yao YP, Kong LM, Zhou AN, Yin JH. Time-dependent unified hardening model: three-dimensional elastoviscoplastic constitutive model for clays. *J Eng Mech, ASCE*. 2015;141(6):441-457.
42. Yin J, Graham J. Elastic viscoplastic modelling of the time-dependent stress-strain behaviour of soils. *Can Geotech J*. 1999;36(4):736-745.
43. Adachi T, Oka F. Constitutive equations for normally consolidated clay based on elasto-viscoplasticity. *Soils Found*. 1982;22(4):57-70.
44. Adachi T, Oka F, Mimura M. Mathematical structure of an overstress elasto-viscoplastic model for clay. *Soils Found*. 1987;27(3):31-42.
45. Perzyna P. The constitutive equations for rate sensitive plastic materials. *Quarterly Appl Math*. 1963;20(4):321-332.
46. Malvern LE. The propagation of longitudinal waves of plastic deformation in a bar of metal exhibiting a strain rate effect. *J Appl Mech*. 1951;18(2):203-208.
47. Yue D, Ling HI, Kaliakin N. Simulating time-independent behavior of clay using an anisotropic elastoplastic-viscoplastic bounding surface model. In: *ASCE 16th Engineering Mechanics Conference*. Seattle, WA; 2003.
48. Kaliakin V, Dafalias Y. Theoretical aspects of the elastoplastic-viscoplastic bounding surface model for cohesive soils. *Soils Found*. 1990;30(3):11-24.
49. Freitas TMB, Potts DM, Zdravkovic L. A time dependent constitutive model for soils with isotach viscosity. *Comput Geotech*. 2011;38(6):809-820.

50. Alshamrani MA, Sture S. A time-dependent bounding surface model for anisotropic cohesive soil. *Soils Found.* 1998;38(1):61-76.
51. Jiang J, Ling HI, Kaliakin VN, Zeng X, Hung C. Evaluation of an anisotropic elastoplastic-viscoplastic bounding surface model for clays. *Acta Geotechnica.* 2017;12(2):335-348.
52. Norton F. *The Creep of Steel at High Temperatures.* NY: Mc Graw Hill Book Company, Inc.; 1929.
53. Nova R. A viscoplastic constitutive model for normally consolidated clay. In: *Proc. IUTAM Conference on Deformation and Failure of Granular Materials, 1982*; 1982:287-295.
54. Yin J, Graham J. Viscous-elastic-plastic modelling of one-dimensional time-dependent behaviour of clays. *Can Geotech J.* 1989;26(2):199-209.
55. Niemunis A. *Extended hypoplastic models for soils.* Germany. Heft 34: Schriftenreihe des Institutes für Grundbau und Bodenmechanik der Ruhr-Universität Bochum. Habilitation; 2003.
56. Kutter BL, Sathialingam N. Elastic-viscoplastic modelling of rate-dependent behaviour of clays. *Géotechnique.* 1992;42(3):427-441.
57. Leoni M, Karstunen M, Vermeer A. Anisotropic creep model. *Géotechnique.* 2008;58(3):215-226.
58. Yin JH, Tong F. Test study and constitutive modelling of the time-dependent stress-strain behavior of soils. In: *Proceedings of the 18th International Conference on Soil Mechanics and Geotechnical Engineering, Paris.* Paris; 2013.
59. Vermeer PA, Neher HP. A soft soil model that accounts for creep. In: 249-262; 1999; Amsterdam, the Netherlands.
60. Fuentes W, Tafili M, Triantafyllidis T. An ISA-plasticity-based model for viscous and non-viscous clays. *Acta Geotechnica.* 2018; 13(2): 367-386. <https://doi.org/10.1007/s11440-017-0548-y>
61. Valanis KC. A theory of viscoplasticity without a yield surface. *Arch Mech.* 1971;23(4):517-533.
62. Niemunis A, Grandas C, Prada L. Anisotropic visco-hypoplasticity. *Acta Geotechnica.* 2009;4(4):293-314.
63. Whittle AJ, Kiavvadas MJ. Formulation of MIT-E3 constitutive model for overconsolidated clays. *J Geotech Eng Div ASCE.* 1994;120(1):173-198.
64. Pestana J, Whittle A. Formulation of a unified constitutive model for clays and sands. *IJNAMG.* 1999;23:1215-1243.
65. Naghdi PM, Murch SA. On the mechanical behavior of viscoelastic/plastic solids. The Plaxis Symposium on Beyond 2000 in Computational Geotechnics. 1999:281-296.
66. Liingaard M, Augustesen A, Lade PV. Characterization of models for time-dependent behavior of soils. *Int J Geomech.* 2004;4(3):157-177.
67. Tatsuoka F, Di Benedetto H, Enomoto T, Kawabe S, Kongkitkul W. Various viscosity types of geomaterials in shear and their mathematical expression. *Soils Found.* 2008;48(1):41-60.
68. Yang C, Carter JP. Isotach elastoplasticity: a case study on Osaka Bay Clay. *Indian Geotech J.* 2017;47(2):161-172.
69. Terzaghi K. *Theoretical Soil Mechanics.* New York: John Wiley and sons; 1943.
70. Butterfield R. A natural compression law for soils. *Géotechnique.* 1979;29(4):469-480.
71. Bauer E. Zum mechanischem Verhalten granularer Stoffe unter vorwiegend oedometrischer Beanspruchung. In: :1-13; 1992; Karlsruhe, Germany. Heft 130.
72. Burland JB. On the compressibility and shear strength of natural clays. *Géotechnique.* 1990;40(3):329-378.
73. Karstunen M, Yin Z. Modelling time-dependent behavior of Murro test embankment. *Géotechnique.* 2010;60(10):735-749.
74. Sivasithamparan N, Karstunen M, Bonnier P. Modelling creep behaviour of anisotropic soft soils. *Comput Geotech.* 2015;69:46-57.
75. Tafili M, Triantafyllidis T. Constitutive model for viscous clays under the ISA framework. In: Triantafyllidis T, ed. *Holistic Simulation of Geotechnical Installation Processes. Lecture Notes in Applied and Computational Mechanics.* Cham: Springer; 2017:324-340.
76. Leinenkugel H. Deformation and strength behaviour of cohesive soils experiments and their physical meaning. PhD Dissertation. University of Karlsruhe. Publications of Institute of Soil and Rock Mechanics. Heft 66; 1976.
77. Olszak W, Perzyna P. The constitutive equations of the flow theory for a nonstationary yield condition. In: *Proc., 11th Int. Congress of Applied Mechanics*; 1966:545-553.
78. Olszak W, Perzyna P. *Stationary and Nonstationary Viscoplasticity.* New York: McGraw-Hill; 1970:53-75.
79. Sekiguchi H. Macrometric approaches—static—intrinsically time dependent constitutive laws of soils. Rep., ISSMFE Subcommittee on Constitutive Laws of Soils and Proc. of Discussion Session 1A, Int. Society of Soil Mechanics and Foundation Engineering, Subcommittee on Constitutive Laws of Soils, 11th ICFMFE, San Francisco. 1985:66-98.
80. Hughes TJR. *Computational Inelasticity.* 7 New York: Springer; 1998.
81. Belytschko T, Liu WK, Moran B, Elkhodary K. *Nonlinear Finite Elements for Continua and Structures.* 2nd ed. Wiley; 2014.
82. Ludwick P. Über den Einfluss der Deformationsgeschwindigkeit bei bleibenden Deformationen mit besonderer Berücksichtigung der Nachwirkungserscheinungen. *Physikalische Zeitschrift.* 1922;10(12):411-417.
83. Prandtl L. Ein Gedanken model zur kinetischen Theorie der festen Körper. *Zeitschrift für Angewandte Mathematik und Mechanik.* 1928;8(2):85-106.
84. Hohenemser K, Prager W. Über die ansätze der mechanik isotroper continua. *Zeitschrift für Angewandte Mathematik und Mechanik.* 1932;12(4):216-226.
85. Sokolovsky VV. Propagation of elastic-viscoplastic waves in bar. *Dokl Akad Nauk SSSR.* 1948;60:775-778.
86. Stolle D, Bonnier P, Vermeer P. A soft soil model and experiences with two integration schemes. In: :123-128; 1999; Amsterdam, the Netherlands. A.A. Balkema.
87. Fuentes W, Hadzibeti M, Triantafyllidis T. Constitutive model for clays under the ISA framework. In: Triantafyllidis T, ed. *Holistic Simulation of Geotechnical Installation Processes. Lecture Notes in Applied and Computational Mechanics.* Switzerland: Springer International Publishing; 2016:115-129.

88. Hadzibeti M Formulation and calibration of a viscous ISA model for clays Master Thesis. Karlsruhe Institute of Technology KIT. Institute of Soil Mechanics and Rock Mechanics IBF 2016.
89. Hibbit Karlsson, Inc. Sorensen. Abaqus 5.6 Theory Manual, 1995.
90. Fellin W, Ostermann A. Consistent tangent operators for constitutive rate equations. *Int J Numer Anal Methods Geomech.* 2002;26(12):1213-1233.
91. Simo JC, Hughes TJR. *Computational Inelasticity*. NY: Springer; 1998.
92. Gudehus G A comparison of some constitutive laws for soils under radially symmetric loading and unloading. In: :1309-1323; 1979.
93. Yuan Y, Whittle AJ, Nash DFT. Model for predicting and controlling creep settlements with surcharge loading. In: Rinaldi VA et al., eds. *Deformation characterisation of geomaterials: proceedings of the 6th international symposium*. IOS Press; 2015:931-938.
94. Imai G, Tanaka Y, Saegusa H. One-dimensional consolidation modeling based on the isotach law for normally consolidated clays. *Soils Found.* 2003;43(54):173-188.
95. Qu G, Hinchberger SD, Lo KY. Evaluation of the viscous behaviour of clay using generalised overstress viscoplastic theory. *Géotechnique.* 2010;60(10):777-789.
96. Watabe Y, Leroueil S. Modeling and implementation of the isotache concept for long-term consolidation behavior. *Int J Geomech.* 2015;15(5):A4014006-1 to A4014006-8.
97. Gudehus G. Comparison of some constitutive laws for soils under radially symmetric loading and unloading. In: *1309-13233-rd International Conference in Aachen*. Rotterdam: Balkema; 1979.
98. Espino E Quasi-statische Untersuchungen zur Elastizität von Sand als Grundlage eines neuen hypoplastischen Stoffmodells Master Thesis. Karlsruhe Institute of Technology KIT. Institute of Soil Mechanics and Rock Mechanics IBF2014; 2014.
99. Niemunis A, Grandas C, Wichtmann T. *Holistic Simulation of geotechnical installation processes—benchmarks and Simulations. Peak stress obliquity in drained and undrained sands. Simulations with neohypoplasticity*. Karlsruhe, Germany: Springer; 2015:85-114.
100. Newland PL, Allely BH. A study of the consolidation characteristics of a clay. *Géotechnique.* 1960;10(2):62-74.
101. Arulanandan K, Shen CK, Young RB. Undrained creep behaviour of a coastal organic silty clay. *Géotechnique.* 1971;21(4):359-375.
102. Walker LK. Undrained creep in a sensitive clay. *Géotechnique.* 1969;19(4):515-529.
103. Augustesen A, Liingaard M, Lade PV. Evaluation of time-dependent behavior of soils. *Int J Geomech.* 2004;4(3):137-156.
104. Luo Q, Chen X. Experimental research on creep characteristics of Nansha soft soil. *Sci World J.* 2014;2014:1-8. <https://doi.org/10.1155/2014/968738>
105. Jamsawang P, Boathong P, Mairaing W, Jongpradist P. Undrained creep failure of a drainage canal slope stabilized with deep cement mixing columns. *Landslides.* 2016;13(5):939-955.
106. Campanella RG, Vaid YP. Triaxial and plane strain creep rupture of an undisturbed clay. *Can Geotech J.* 1974;11(1):1-10.
107. Faruque MO, Asce AM. Modeling of undrained creep of normally consolidated clay. *J Eng Mech, ASCE.* 1986;112(10):1007-1020.
108. Bhat DR, Bhandari NP, Yatabe R, Tiwari RC. Prediction of large-scale landslide based on tertiary creep test by modified ring shear apparatus. In: *Proceedings of the thirteenth international summer symposium, Japan*. Japan; 2011:179-182.
109. Bhat DR, Bhandary NP, Yatabe R. Residual-state creep behavior of typical clayey soils. *Nat Hazards.* 2013;69(3):2161-2178.
110. Lacasse S, Berre T Simulating time-independent behavior of clay using an anisotropic elastoplastic-viscoplastic bounding surface model. In: Millpress Science Publishers/IOS Press; 2005-2006. <https://doi.org/10.3233/978-1-61499-656-9-531>
111. Ting JM. Tertiary creep model for frozen sands. *J Geotech Eng.* 1983;109(7):932-945.
112. Vaid YP, Campanella RG. Time-dependent behaviour of undisturbed clay. *ASCE J Geot Eng Div.* 1977;103(GT7):693-709.

How to cite this article: Tafili M, Fuentes W, Triantafyllidis T. A comparative study of different model families for the constitutive simulation of viscous clays. *Int J Numer Anal Methods Geomech.* 2020;1-35. <https://doi.org/10.1002/nag.3024>

APPENDIX A: SHORT GUIDE FOR THE MATERIAL PARAMETER DETERMINATION

The following lines give a short guide for the determination of the material parameters.

- The compression and swelling index, denoted with λ and κ , respectively, are calibrated with isotropic or oedometric compression curves. A compression path with constant strain rate is expected to approach asymptotically to a line in the $e - \ln(p)$ space with slope equal to λ . Parameter κ is calibrated at the slope of an unloading path in the $e - \ln(p)$ space.
- The critical state slope M is calibrated through the critical state friction angle φ_c through the relation $M = 6 \sin \varphi_c / (3 - \sin \varphi_c)$.
- The reference strain rate D_r is recommended to be set to the volumetric strain rate of a known experimental curve $D_r = \dot{\epsilon}_v$.

- The characteristic void ratio e_{ref0} is found by adjusting the reference isotach, described by $e = e_{\text{ref0}} - \lambda \ln(p)$, to the compression curve with $\dot{\epsilon}_v = D_r$.
- The viscosity index I_v can be found through two isotachs under isotropic compression ($q = 0$). To that end, consider the overconsolidation ratios of OCR_a and OCR_b and volumetric strain rates of $\dot{\epsilon}_{v,a}$ and $\dot{\epsilon}_{v,b}$ for the two isotachs, respectively. One may use the relation for the NVP model (see Equation 71):

$$I_v = \ln \left(\frac{\text{OCR}_b}{\text{OCR}_a} \right) / \ln \left(\frac{\dot{\epsilon}_{v,a}}{\dot{\epsilon}_{v,b}} \right). \quad (\text{A1})$$

- The poisson ratio ν can be adjusted to match the stiffness of an undrained triaxial test. At the q vs. ϵ_1 space, the initial stiffness of an undrained triaxial test is equal to $3G$, where G is related to ν through Equations 24. A simple trial and error procedure may be also useful to find a ν which renders accurate simulations for undrained tests.

APPENDIX B: REQUIRED DERIVATIVES

In the following lines, the required derivatives for the semi-implicit integration of the viscoplastic strain rate $\dot{\epsilon}^{vp}$ for the OS and VP models and viscous strain rate $\dot{\epsilon}^{vis}$ for the VHP model are given.

B.1 | OVP and NVP models

For these models, the derivative $(\partial \dot{\epsilon}^{vp})/(\partial \boldsymbol{\sigma})$ is found as follows:

$$\frac{\partial \dot{\epsilon}^{vp}}{\partial \boldsymbol{\sigma}} = \frac{\partial \dot{\epsilon}^{vp}}{\partial p} \otimes \frac{\partial p}{\partial \boldsymbol{\sigma}} + \frac{\partial \dot{\epsilon}^{vp}}{\partial q} \otimes \frac{\partial q}{\partial \boldsymbol{\sigma}}, \quad (\text{B1})$$

with

$$\frac{\partial \dot{\epsilon}^{vp}}{\partial p} = \frac{D_r (M^2 p^2 - q^2) (1 + q^2 / (M^2 p^2))^{1/I_v}}{I_v p (p_{ei}/p)^{1/I_v} (M^2 p^2 + q^2)}, \quad (\text{B2})$$

$$\frac{\partial \dot{\epsilon}^{vp}}{\partial q} = \frac{2 D_r q (1 + q^2 / (M^2 p^2))^{1/I_v}}{I_v (p_{ei}/p)^{1/I_v} (M^2 p^2 + q^2)}. \quad (\text{B3})$$

Note that the third stress invariant has not been considered.

B.2 | VHP model

For the VHP model, the derivative $(\partial \dot{\epsilon}^{vis})/(\partial \boldsymbol{\sigma})$ is found as follows:

$$\frac{\partial \dot{\epsilon}^{vis}}{\partial \boldsymbol{\sigma}} = \frac{\partial \dot{\epsilon}^{vis}}{\partial \text{OCR}_{3D}} \otimes \left(\frac{\partial \text{OCR}_{3D}}{\partial p} \frac{\partial p}{\partial \boldsymbol{\sigma}} + \frac{\partial \text{OCR}_{3D}}{\partial q} \frac{\partial q}{\partial \boldsymbol{\sigma}} \right), \quad (\text{B4})$$

with

$$\frac{\partial \dot{\epsilon}^{vis}}{\partial \text{OCR}_{3D}} = \lambda \text{OCR}_{3D}^{1-1/I_v}, \quad \mathbf{m} \quad (\text{B5})$$

$$\frac{\partial \text{OCR}_{3D}}{\partial p} = - \frac{f_b^2 M c^2 p^2 p_{ei} + (2 p - 3 p_{ei}) q^2}{f_b^2 M^2 p^4}, \quad (\text{B6})$$

$$\frac{\partial \text{OCR}_{3D}}{\partial q} = \frac{2 (p - p_{ei}) q}{f_b^2 M^2 p^3}, \quad (\text{B7})$$

$$\frac{\partial p}{\partial \boldsymbol{\sigma}} = - \frac{1}{3} \mathbf{1}, \quad \frac{\partial q}{\partial \boldsymbol{\sigma}} = \frac{3}{2} \boldsymbol{\sigma}^*. \quad (\text{B8})$$

The derivative $(\partial \dot{\epsilon}^{vis})/(\partial \dot{\epsilon})$ is found as follows:

$$\frac{\partial \dot{\epsilon}^{vis}}{\partial \dot{\epsilon}} = \frac{\partial \dot{\epsilon}^{vis}}{\partial e} \otimes \frac{\partial e}{\partial \dot{\epsilon}} = (1 + e) \frac{\partial \dot{\epsilon}^{vis}}{\partial e} \otimes \mathbf{1}, \quad (\text{B9})$$

and

$$\frac{\partial \dot{\boldsymbol{\varepsilon}}^{vis}}{\partial e} = \frac{\partial \dot{\boldsymbol{\varepsilon}}^{vis}}{\partial OCR_{3D}} \left(\frac{\partial OCR_{3D}}{\partial p_{ei}} \frac{\partial p_{ei}}{\partial e} + \frac{\partial OCR_{3D}}{\partial f_b} \frac{\partial f_b}{\partial e} \right), \quad (B10)$$

with

$$\frac{\partial OCR_{3D}}{\partial p_{ei}} = \frac{1}{p} - \frac{1}{p} \left(\frac{\|\mathbf{r}\|}{f_b} \right)^2, \quad \frac{\partial OCR_{3D}}{\partial f_b} = -\frac{2}{f_b} \left(1 - \frac{p_{ei}}{p} \right) \left(\frac{\|\mathbf{r}\|}{f_b} \right)^2, \quad (B11)$$

$$\frac{\partial p_{ei}}{\partial e} = -\frac{1}{\lambda} \exp\left(\frac{e_{i0} - e}{\lambda}\right), \quad \frac{\partial f_b}{\partial e} = -\frac{n_f f_{b0} (e/e_{i0})^{n_f - 1}}{2 e_{i0} \sqrt{1 - (e/e_{i0})^{n_f}}}. \quad (B12)$$

APPENDIX C: PROGRAMMING THE CREEP RUPTURE CONDITION FOR THE VHP MODEL

For triaxial conditions, we may simplify the VHP model to the following matricial form:

$$[\dot{\boldsymbol{\sigma}}] = [E] \left[[\dot{\boldsymbol{\varepsilon}}] - Y[\mathbf{m}]\|\dot{\boldsymbol{\varepsilon}}\| \right] + [\dot{\boldsymbol{\sigma}}^{vp}], \quad (C1)$$

whereby

$$[\dot{\boldsymbol{\sigma}}] = \begin{bmatrix} \dot{\sigma}_{11} \\ \dot{\sigma}_{22} \\ \dot{\sigma}_{33} \end{bmatrix} = \begin{bmatrix} -\dot{p} + 2/3\dot{q} \\ \dot{q} - 1/3\dot{q} \\ \dot{q} - 1/3\dot{q} \end{bmatrix}, \quad [\dot{\boldsymbol{\varepsilon}}] = \begin{bmatrix} \dot{\varepsilon}_{11} \\ \dot{\varepsilon}_{22} \\ \dot{\varepsilon}_{33} \end{bmatrix} = \begin{bmatrix} -1/3\dot{\varepsilon}_v - \dot{\varepsilon}_s \\ -1/3\dot{\varepsilon}_v + \dot{\varepsilon}_s \\ -1/3\dot{\varepsilon}_v + \dot{\varepsilon}_s \end{bmatrix} \quad (C2)$$

For the same conditions, the elastic stiffness matrix $[E]$ may be written as follows:

$$[E] = K \begin{bmatrix} 1 & 1 & 1 \\ 1 & 1 & 1 \\ 1 & 1 & 1 \end{bmatrix} + 2G \begin{bmatrix} 2/3 & -1/3 & -1/3 \\ -1/3 & 2/3 & -1/3 \\ -1/3 & -1/3 & 2/3 \end{bmatrix} - \frac{K}{\sqrt{3}} ([\mathbf{r}][\mathbf{1}]^T + [\mathbf{1}][\mathbf{r}]^T), \quad (C3)$$

and the stress ratio is computed as

$$[\mathbf{r}] = \frac{1}{p} \begin{bmatrix} 2/3 & -1/3 & -1/3 \\ -1/3 & 2/3 & -1/3 \\ -1/3 & -1/3 & 2/3 \end{bmatrix} \begin{bmatrix} -p + 2/3q \\ q - 1/3q \\ q - 1/3q \end{bmatrix} \quad (C4)$$

The hypoplastic flow rule is computed as

$$[\mathbf{m}] = \frac{1}{\sqrt{3}} \frac{-1/2\sqrt{2/3}M_c(1 - q/p/M_c)[\mathbf{1}] + [\mathbf{r}]/(\sqrt{2/3}M_c)}{\| -1/2\sqrt{2/3}M_c(1 - q/p/M_c)[\mathbf{1}] + [\mathbf{r}]/(\sqrt{2/3}M_c) \|}. \quad (C5)$$

The nonlinear tensor $[\mathbf{N}]$ is

$$[\mathbf{N}] = -Y([E][\mathbf{m}]). \quad (C6)$$

whereby $[\mathbf{n}]$ represents the unit vector pointing in triaxial compression conditions

$$[\mathbf{n}] = \frac{1}{\sqrt{2}} \begin{bmatrix} -1 \\ 0.5 \\ 0.5 \end{bmatrix} \quad (C7)$$

The continuum Jacobian matrix is

$$[J] = [E] + [\mathbf{N}].[n]^T. \quad (C8)$$

We now transform the continuum Jacobian matrix $[J]$ under Roscoe components by performing the following operations. Let denote $[M_s]$ and $[M_e]$ the transformation matrices, such that $[t] = [M_s][\boldsymbol{\sigma}]$ and $[d] = [M_e][\boldsymbol{\varepsilon}]$, and $[t] = [p, q, 0]^T$ and $[d] = [\varepsilon_v, \varepsilon_s, 0]^T$ are the Roscoe stress and strain components vectors, respectively. Hence, the transformation matrices $[M_s]$ and $[M_e]$ read

$$[M_s] = \begin{bmatrix} -1/3 & -1/3 & -1/3 \\ -1 & 1/2 & 1/2 \\ 0 & -1 & 1 \end{bmatrix} \quad \text{and} \quad [M_e] = \begin{bmatrix} -1 & -1 & -1 \\ -2/3 & 1/3 & 1/3 \\ 0 & -1/2 & 1/2 \end{bmatrix} \quad (C9)$$

Let $[E^{pq}]$ denote the continuum jacobian matrix under Roscoe variables, such that

$$[t] = [E^{pq}][d] + [t^{vp}]. \quad (C10)$$

Considering the relations above, one can show that the following identity holds:

$$[E^{pq}] = [M_s][E][M_e]^{-1}. \quad (C11)$$

The undrained creep rupture condition is satisfied if the component $[E^{pq}]_{(2,2)}$ vanishes:

$$[E^{pq}]_{(2,2)} = 0 \quad (\text{undrained rupture condition}). \quad (C12)$$

APPENDIX D: MATHEMATICA SCRIPT FOR THE CALIBRATION OF E_{I0}

In order to compare the VHP and UH models with the VP model, we calibrated them to have the same reference isotach. For this purpose, first the overconsolidation ratios at this reference isotach are calculated. VP model possess $OCR = 1$ at this $\dot{\epsilon} = D_r$ - line. The value of OCR for the other models is obtained by solving a nonlinear equation, eg, with a Mathematica script. After this, the equivalent void ratio is obtained from the cam clay equation for the normal consolidation line (in this case, reference isotach). The Mathematica scripts for these steps read the follow lines:

```
(*VHP model*)
(*Parameters*)
ClearAll[der, Y0max, kappa, lambda];

(*DEFINE PARAMETERS*)
Calpha = 0.005; (*Creep index*)
lambda = 0.1; (*compression index*)
kappa = 0.01; (*swelling index*)
NN2 = 1.2; (*void ratio of the reference Isotach at p=1 kPa*)
Iv = Calpha/lambda // N; (*viscosity index*)
rk = lambda/kappa;
Y0max = (rk - 1)/(rk + 1) // N;
der = 1.0 * 10(-6);

nn1 = nn /. FindRoot[(1 - Y0max)der == (1 - Y0max * (1/nn)2)der - Calpha * (1/nn)(1/Iv)Sqrt[3], nn, 0.1];
Print["N from OCR=1 Linie:"
NN2 - lambda*Log[1/nn1]

(*UH model*)
(*Parameters*)
ClearAll[der, Y0max, kappa, lambda];

(*DEFINE PARAMETERS*)
Calpha = 0.005; (*Creep index*)
lambda = 0.1; (*compression index*)
kappa = 0.01; (*swelling index*)
NN2 = 1.2; (*void ratio of the reference Isotach at p=1 kPa*)
Iv = Calpha/lambda; (*viscosity index*)
M = 1.35;
chi = M2/(12 * (3 - M));
Mf = 6*(Sqrt[(chi/nn*(1 + chi/nn))] - chi/nn);
der = 1.0 * 10(-6);
```

$$a = 1 + ((\lambda - \kappa)/\kappa) * (M/M_f)^4;$$

$$nn1 = nn /$$

$$FindRoot[der/\lambda == der/\kappa/a - C\alpha * nn^{(1/lv)}/(1 + NN2)/\kappa/a, nn, 0.1];$$

Print["N from OCR=1 Linie:"]

$$NN2 - \lambda * \text{Log}[nn1]$$